

Connecting the Dots: Towards Continuous Time Hamiltonian Monte Carlo

Tore Selland Kleppe*

July 19, 2022

Abstract

Continuous time Hamiltonian Monte Carlo is introduced, as a powerful alternative to Markov chain Monte Carlo methods for continuous target distributions. The method is constructed in two steps: First Hamiltonian dynamics are chosen as the deterministic dynamics in a continuous time piecewise deterministic Markov process. Under very mild restrictions, such a process will have the desired target distribution as an invariant distribution. Secondly, the numerical implementation of such processes, based on adaptive numerical integration of second order ordinary differential equations is considered. The numerical implementation yields an approximate, yet highly robust algorithm that, unlike conventional Hamiltonian Monte Carlo, enables the exploitation of the complete Hamiltonian trajectories (hence the title). The proposed algorithm may yield large speedups and improvements in stability relative to relevant benchmarks, while incurring numerical errors that are negligible relative to the overall Monte Carlo errors.

Keywords: Hamiltonian Monte Carlo, MCMC, Piecewise deterministic processes, Runge-Kutta-Nystrom

1 Introduction

By now, Markov chain Monte Carlo (MCMC) methods and their widespread application in Bayesian statistics need no further introduction (see e.g. Gelman et al., 2014; Robert and Casella, 2004). This paper introduces a, to the author's knowledge, new class of approximate MCMC-like methods applicable for challenging and high-dimensional estimation problems.

The current state of the art general purpose MCMC algorithm for continuous target distributions is Hamiltonian Monte Carlo (HMC) (see Neal, 2010, for an introduction). HMC methods come in many

*Department of Mathematics and Physics, University of Stavanger, 4036 Stavanger, Norway. Email: tore.kleppe@uis.no

incarnations (see e.g. Girolami and Calderhead, 2011; Fang et al., 2014; Bou-Rabee and Sanz-Serna, 2017, and references therein), but arguably the most successful instance is the no-U-turn sampler (Hoffman and Gelman, 2014), as a variant of the no-U-turn sampler is the main sampling algorithm of the widely used Bayesian statistical software Stan (Carpenter et al., 2017).

HMC methods rely on defining a synthetic Hamiltonian (i.e. energy preserving) physical system related to the target distribution in consideration. Subsequently, the dynamics of the system, satisfying a certain system of ordinary differential equations (ODEs), is numerically simulated to form the proposal mechanism for the HMC MCMC algorithm. Provided the numerical integrator employed to simulate the dynamics is time-reversible and volume preserving (i.e., symplectic), the accept probability associated with such a proposal has a simple and computationally convenient form. In fact, only rather crude simulation of the dynamics is required, as any incurred numerical errors are exactly corrected in the accept/reject step.

However, with symplecticity comes rather strict requirements on the numerical integration process. In particular, the adaptive step size selection (or similar mechanisms) commonly associated with practical numerical ODE integration (see e.g. Hairer et al., 1993; Press et al., 2007) breaks the symplectic nature of the numerical integration. Fixed step sizes work very well for close to Gaussian target distributions. However, for more “irregular” distributions, a fixed step size strategy may either lead to a failure to explore the complete target distribution, or highly inefficient integration as the fixed step size must account for the most “extreme” parts of the target distribution (see e.g. Kleppe, 2018, Figure 8, Stan, for an example where fixed time step integrators fail to explore the target).

The first contribution of this work is the consideration of adaptive, highly precise, generally non-symplectic integrators (see e.g. Hairer et al., 1993) for HMC-like statistical computing. As will be clear from this paper, such precise integration procedures may be used uncorrected (i.e. no accept/reject step or similar) as they may arbitrarily accurately represent the true underlying Hamiltonian dynamics. In practice, even for rather lax error tolerances, the incurred biases are close to imperceivable relative to the Monte Carlo variation of the overarching MCMC procedure. Further, this development allows the leveraging of the large numerical ODE toolbox to obtain a very versatile and computationally fast and stable methodology.

Having taken the leap from crude symplectic integrators to more precise integration seeking to faithfully represent the true dynamics, the second main contribution of this paper is the application of such precisely integrated dynamics as the deterministic dynamics within currently popular continuous time piecewise deterministic (Markov) processes (PDPs) (see e.g. Davis, 1993; Fearnhead et al., 2018; Vanetti et al., 2017, and references therein). The resulting PDP processes are referred to as continuous time Hamiltonian Monte Carlo (CTHMC) processes. PDPs are continuous time, generally time-irreversible, stochastic processes where “events” occur at random times according to some event intensity rate, say λ . Between the events, the process

follows some deterministic dynamics, and at events, the state of the process is randomly altered according to some Markov kernel, say Q .

Most current PDP implementations, such as the Bouncy Particle Sampler (Bouchard-Côté et al., 2018), the Zig-Zag process (Bierkens et al., 2019; Cotter et al., 2020), and the Coordinate Sampler (Wu and Robert, 2020), rely linear deterministic dynamics that a priori do not reflect the target distribution. Further, Vanetti et al. (2017, Section 2.4) consider dynamics stemming from a linear system of ODEs. Common for the mentioned approaches is that the event rate λ is the main vehicle for ensuring that the resulting PDP has any given target distribution as a stationary distribution. Consequently, the selection of event rate is strongly constrained. For CTHMC processes on the other hand, the deterministic dynamics conserve the target distribution, and consequently both λ and Q may be chosen much more freely. This flexibility may be leveraged to select CTHMC processes more optimized for the estimation problem at hand. A further benefit of using conserving dynamics is that CTHMC is likely to scale to very high-dimensional problems. Finally, the proposed methodology does not rely on a-priori given model-dependent bounds on the event rate, as the simulation of the underlying non-homogenous Poisson process is straight forward within the current numerical framework.

Using (the in theory exact-, and in practice, precisely approximated) Hamiltonian dynamics within the PDP framework offer several advantages relative to the application within conventional discrete time HMC-MCMC. In particular, certain moments for certain target distributions may be estimated extremely efficiently relative to HMC-MCMC. This observation is related to that unlike conventional HMC-MCMC, CTHMC processes may exploit the complete simulated Hamiltonian trajectories rather than only the initial and final configurations.

This paper is laid out as follows: Firstly, it provides theory for the construction of a large class of CTHMC processes for a given target distribution and discusses some of the properties of the simplest subclass of such processes (Section 3). Secondly, it discusses a practical numerical implementation of such processes, in particular the effect on output of using this numerical implementation rather than its theoretical counterpart (Section 4). Thirdly, it shows that for challenging target distributions, the proposed method may be both more reliable and efficient when benchmarked against Stan (Sections 5 and 6). Finally, Section 7 provides discussion. The complete set of source code underlying this paper is available at <https://github.com/torekleppe/PDPHMCpaperCode>.

2 Background

This section provides some background and fixes notation for subsequent use. Throughout this paper, a target distribution with density $\pi(\mathbf{q})$, $\mathbf{q} \in \Omega \subseteq \mathbb{R}^d$ with an associated density kernel $\tilde{\pi}(\mathbf{q})$ which can be evaluated point-wise. The gradient/Jacobian operator of a function with respect to some variable, say \mathbf{x} , is denoted by $\nabla_{\mathbf{x}}$. Time-derivatives are denoted using the conventional dot-notation, i.e. $\dot{f}(\tau) = \frac{d}{d\tau}f(\tau)$, $\ddot{f}(\tau) = \frac{d^2}{d\tau^2}f(\tau)$ for some function $f(\tau)$ evolving over time τ .

In the remainder of this section, Hamiltonian mechanics, HMC and PDPs are briefly reviewed in order to fix notation and provide the required background. The reader is referred to Goldstein et al. (2002); Leimkuhler and Reich (2004) and Neal (2010) for more detailed introductions to Hamiltonian mechanics and HMC. Davis (1984, 1993) for consider PDPs in general and Fearnhead et al. (2018); Vanetti et al. (2017) give details for Monte Carlo applications of PDPs.

2.1 Elements of Hamiltonian mechanics

Hamiltonian Monte Carlo methods rely on specifying a physical system and use the dynamics of this system to propose transitions. The state $\mathbf{z} = [\mathbf{q}^T, \mathbf{p}^T]^T \in \mathbb{R}^{2d}$ of the system is characterized by a position coordinate $\mathbf{q} \in \mathbb{R}^d$ and a momentum coordinate $\mathbf{p} \in \mathbb{R}^d$. The system itself is conventionally specified in terms of the Hamiltonian $\mathcal{H}(\mathbf{z}) = \mathcal{H}(\mathbf{q}, \mathbf{p})$ which gives the total energy of the system for a given state \mathbf{z} . Throughout this work, physical systems with Hamiltonian given as

$$\mathcal{H}(\mathbf{q}, \mathbf{p}) = -\log \tilde{\pi}(\mathbf{q}) + \frac{1}{2}\mathbf{p}^T \mathbf{M}^{-1}\mathbf{p}, \quad (1)$$

are considered. Here $\mathbf{M} \in \mathbb{R}^{d \times d}$ is a symmetric, positive definite (SPD) mass matrix which is otherwise specified freely. The time-evolution of the system is given by Hamilton's equations $\dot{\mathbf{q}}(\tau) = \nabla_{\mathbf{p}}\mathcal{H}(\mathbf{q}(\tau), \mathbf{p}(\tau))$, $\dot{\mathbf{p}}(\tau) = -\nabla_{\mathbf{q}}\mathcal{H}(\mathbf{q}(\tau), \mathbf{p}(\tau))$, which for Hamiltonian (1) reduces to:

$$\dot{\mathbf{z}}(\tau) = \begin{bmatrix} \dot{\mathbf{q}}(\tau) \\ \dot{\mathbf{p}}(\tau) \end{bmatrix} = \begin{bmatrix} \mathbf{M}^{-1}\mathbf{p}(\tau) \\ \nabla_{\mathbf{q}} \log \tilde{\pi}(\mathbf{q}(\tau)) \end{bmatrix} \quad (2)$$

The flow associated with (2) is denoted by $\varphi_{\tau}(\cdot)$, and is defined so that $\mathbf{z}(\tau + s) = \varphi_s(\mathbf{z}(\tau))$ solves (2) for any scalar time increment s , initial time τ and initial configuration $\mathbf{z}(\tau)$. The flow can be shown to be

- Energy preserving, i.e. $\frac{\partial}{\partial \tau}\mathcal{H}(\varphi_{\tau}(\mathbf{z})) = 0$ for all admissible \mathbf{z} ,
- Volume preserving, i.e. $|\nabla_{\mathbf{z}}\varphi_{\tau}(\mathbf{z})| = 1$ for each fixed τ and all admissible \mathbf{z} ,

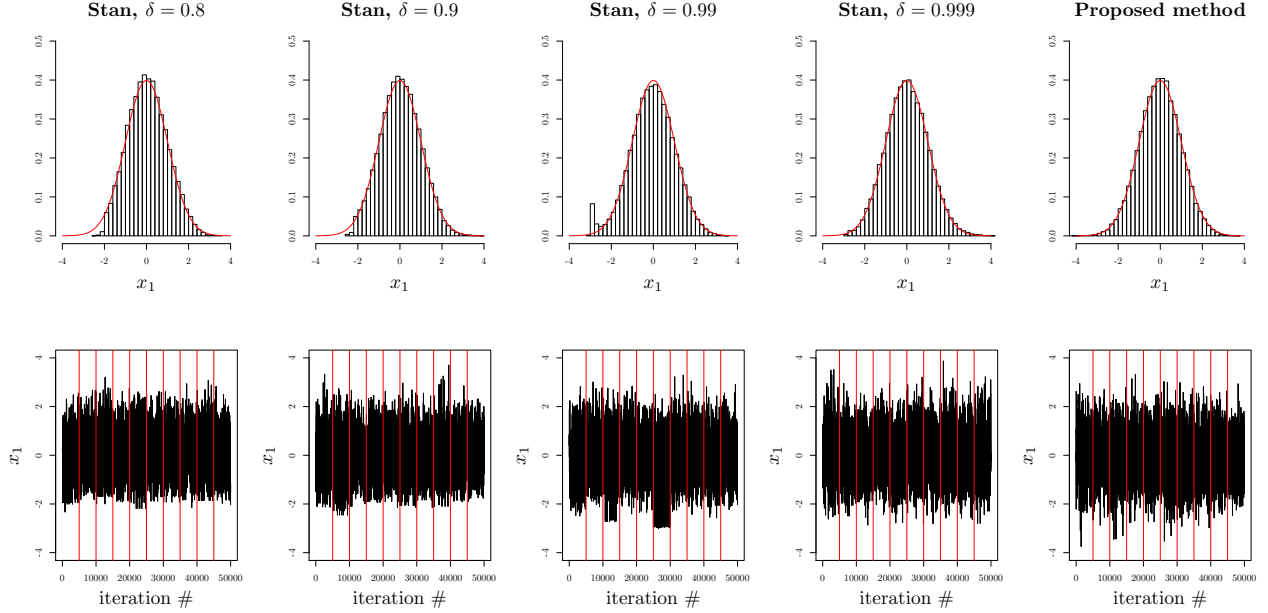


Figure 1: Density-scaled histograms and trace-plots (thinned to show every 10 samples) of MCMC output for marginally standard Gaussian \mathbf{q}_1 -marginal under the “funnel”-model $\mathbf{q}_1 \sim N(0, 1)$, $\mathbf{q}_2 | \mathbf{q}_1 \sim N(0, \exp(3\mathbf{q}_1))$. Further details on this experiment can be found in Section 5.1. Each case is based on 5000 samples from 10 independent replica. In the histograms, the red line gives the true $N(0, 1)$ density, whereas samples between two vertical red lines in the trace plots correspond to one simulation replica. The four left-most panels are based on Stan output with different values of the accept rate target δ . In practice, higher values of δ corresponds to smaller integrator step sizes and more integrator steps per produced sample. The right-most panel shows output for the proposed methodology using constant event rates. For both Stan and the proposed methodology, an identity mass matrix was employed.

- Time reversible, which in the present context is most conveniently formulated via that $\mathbf{T}_\tau = \mathbf{R} \circ \varphi_\tau$ is an involution so that $\mathbf{T}_\tau \circ \mathbf{T}_\tau$ is the identity operator. The momentum flip operator $\mathbf{R} = \text{diag}(\mathbf{I}_d, -\mathbf{I}_d)$ effectively reverses time.

2.2 Hamiltonian Monte Carlo

In the context of statistical computing, Hamiltonian dynamics has attracted much attention the last decade. This interest is rooted in that the flow φ_τ of (2) (and also associated involution \mathbf{T}_τ) exactly preserves the Boltzmann distribution

$$\rho(\mathbf{z}) = \rho(\mathbf{q}, \mathbf{p}) \propto \exp(-\mathcal{H}(\mathbf{q}, \mathbf{p})) \propto \pi(\mathbf{q})\mathcal{N}(\mathbf{p}|\mathbf{0}_d, \mathbf{M}), \quad (3)$$

associated with \mathcal{H} . I.e., for each fixed time increment τ , $\varphi_\tau(\mathbf{z}) \sim \rho$ whenever $\mathbf{z} \sim \rho$. It is seen that the target distribution is the \mathbf{q} -marginal of the Boltzmann distribution. Thus, a hypothetical MCMC algorithm targeting (3), and producing samples $\mathbf{z}_{(i)} = (\mathbf{q}_{(i)}^T, \mathbf{p}_{(i)}^T)^T$, would involve the Boltzmann distribution-preserving

steps:

- Sample $\mathbf{p}_* \sim N(\mathbf{0}_d, \mathbf{M})$ and set $\mathbf{z}_* = (\mathbf{q}_{(i-1)}^T, \mathbf{p}_*^T)^T$.
- For some suitable time increment s , $\mathbf{z}_{(i)} = \varphi_s(\mathbf{z}_*)$.

Subsequently, the momentum samples, $\mathbf{p}_{(i)}$, may be discarded to obtain samples targeting $\pi(\mathbf{q})$ only. More elaborate HMC-type algorithms such as e.g. Hoffman and Gelman (2014); Bou-Rabee and Sanz-Serna (2017) may be thought of as clever ways of randomizing the time increments in the above algorithm.

For all but the most analytically tractable target distributions, the flow associated with Hamilton’s equations is not given in closed form, and hence it must be integrated numerically for the practical implementation of the above MCMC sampler. Provided a time-reversible integrator is employed for this task, the numerical error incurred in the second step of the above MCMC algorithm can be exactly corrected using an accept/reject step (Fang et al., 2014), but the accept probability may be computationally demanding. If the employed integrator is also volume preserving (i.e. symplectic) (see e.g. Leimkuhler and Reich, 2004), the accept-probability depends only on the values of the Hamiltonian before and after the integration. This simplification has led to the widespread application of the symplectic leap-frog (or Størmer-Verlet) integrator in HMC implementations such as e.g. Stan (Stan Development Team, 2017).

Requiring the integrator to be time reversible and symplectic imposes rather strict restrictions on the integration process. In particular the application of adaptive (time-)step sizes, which is an integral part of any modern general purpose numerical ODE code, is at best difficult to implement (see Leimkuhler and Reich, 2004, Chapter 9 for discussion of this problem) while maintaining time-reversible and symplectic properties.

Figure 1 illustrates the effect of using fixed step sizes for the funnel-type distribution $q_1 \sim N(0, 1)$, $q_2|q_1 \sim N(0, \exp(3q_1))$ (further details on this experiment can be found in Section 5.1). In the four left panels, output using the fixed step size integrator in Stan are depicted for various accept rate targets δ which has a default value of 0.8. In practice, higher values of δ correspond to higher fidelity integration with smaller integrator step sizes and more integrator steps per produced sample. It is seen that even with very small step sizes, Stan fails to properly represent the left-hand tail of q_1 (which imply a very small scale in the q_2). In particular, in the $\delta = 0.999$ case, the smallest produced sample out 50000 is ≈ -3.026 . In an iid $N(0, 1)$ sample of this size, one would expect around 62 samples smaller than this value.

Also included in Figure 1 are results from a variant of the proposed methodology (see Section 5.1 for details), which is based on adaptive numerical integrators. The method shows no such pathologies, and in particular the number of samples below the smallest $\delta = 0.999$ Stan sample was 70.

2.3 Piecewise deterministic processes

Recently, continuous time piecewise deterministic processes (PDP) (see e.g. Davis, 1984, 1993) have been considered, as alternatives to discrete time Markov chains produced by conventional MCMC methods. PDP may be employed for simulating dependent samples, or more generally continuous time trajectories with a given marginal probability distribution (see Fearnhead et al., 2018, and references therein). As the name indicate, PDPs follow a deterministic trajectory between events occurring at stochastic times. At events, the state is updated in a stochastic manner.

Following Fearnhead et al. (2018), a PDP, say $\mathcal{Z}(t) \in \mathbb{R}^D$, $t \in [0, \infty)$, is specified in terms of three components (Φ, λ, Q) :

- Deterministic dynamics on *time intervals where events do not occur*, specified in terms of a set of ODEs: $\dot{\mathcal{Z}}(t) = \Phi(\mathcal{Z}(t))$.
- A non-negative event rate $\lambda(\mathcal{Z}(t))$, depending only on the current state of the process, so that the probability of an event between times t and $t + r$, $r \geq 0$ is $\lambda(\mathcal{Z}(t))r + o(r)$ for small r .
- Finally, a “transition distribution at events” $Q(\cdot|\mathcal{Z}(t-))$. Suppose an event occurs at time t , and $\mathcal{Z}(t-)$ is the state immediately before time t . Then the $\mathcal{Z}(t)$ will be drawn randomly with density $Q(\cdot|\mathcal{Z}(t-))$.

Note that in what follows, t is used to denote PDP process time, whereas τ is used for Hamiltonian dynamics time. Let Ξ_τ be the flow associated with Φ . In order to simulate from a PDP, suppose first that $\mathcal{Z}(0)$ has been set to some value, and that t is initially set to zero. Then the following three steps are repeated until $t > T$ where T is the desired length of the PDP trajectory:

- Simulate a new $u \sim \text{Exp}(1)$ and subsequently the time-increment until next event v , which obtains as the solution in v to

$$\Lambda(v; \mathcal{Z}(t)) = u, \text{ where } \Lambda(v; \mathbf{z}) = \int_0^v \lambda(\Xi_s(\mathcal{Z}(t))) ds. \quad (4)$$
- Set $\mathcal{Z}(t + s) = \Xi_s(\mathcal{Z}(t))$ for all $s \in [0, v)$, and $\mathcal{Z}^* = \Xi_v(\mathcal{Z}(t))$.
- Set $t \leftarrow t + v$ and simulate $\mathcal{Z}(t) \sim Q(\cdot|\mathcal{Z}^*)$.

An invariant distribution of the process $\mathcal{Z}(t)$, say $p(\mathbf{z})$, will satisfy the time-invariant Fokker-Planck/Kolmogorov forward equation (Fearnhead et al., 2018)

$$\sum_{i=1}^D \frac{\partial}{\partial z_i} [\Phi_i(\mathbf{z})p(\mathbf{z})] = \int p(\mathbf{z}')\lambda(\mathbf{z}')Q(\mathbf{z}|\mathbf{z}')d\mathbf{z}' - p(\mathbf{z})\lambda(\mathbf{z}), \quad (5)$$

for all admissible states \mathbf{z} . For continuous time Monte Carlo applications, one therefore seek combinations of (Φ, λ, Q) so that the desired target distribution is an invariant distribution $p(\mathbf{z})$.

Provided such a combination has been found, discrete time Markovian samples $\mathbf{z}_{(i)} = \mathcal{Z}(\Delta i)$, for some sample spacing $\Delta > 0$, may be used in the same manner as regular MCMC samples in order to characterize the invariant distribution. In addition, by letting the sample spacing $\Delta \rightarrow 0$, moments under the invariant distribution may also be obtained by utilizing the complete trajectory of the PDP, i.e.

$$\frac{1}{T} \int_0^T g(\mathcal{Z}(t)) dt \xrightarrow{T \rightarrow \infty} \int g(\mathbf{z}) p(\mathbf{z}) d\mathbf{z}, \quad (6)$$

for some function g .

3 Continuous time HMC

In this paper, PDPs with deterministic dynamics corresponding to (appropriately chosen) Hamiltonian dynamics (2) between events are considered. In this section, analysis is performed with the premise that the Hamiltonian dynamics is available in closed form. In this case, it is straight forward to show that for a large class of combinations of (λ, Q) , such PDPs will have the Boltzmann distribution (3) as a stationary distribution. In practice, the Hamiltonian flow is implemented using high precision adaptive numerical methods (to be discussed in Section 4.1), to obtain a robust and accurate, but nevertheless *approximate* versions of these PDPs.

The continuous time HMC process targeting $\rho(\mathbf{z})$ is constructed as follows; set $D = 2d$, $\mathbf{z} = [\mathbf{q}^T, \mathbf{p}^T]^T$, and let the deterministic dynamics be the Hamiltonian dynamics $\Phi(\mathbf{z}) = \left[[\mathbf{M}^{-1}\mathbf{p}]^T, [\nabla_{\mathbf{q}} \log \tilde{\pi}(\mathbf{q})]^T \right]^T$, $\Xi_{\tau} = \varphi_{\tau}$. Further, the notation $\mathcal{Q}(t)$ and $\mathcal{P}(t)$ are used for position- and momentum sub-vectors of $\mathcal{Z}(t)$ respectively, i.e. $\mathcal{Z}(t) = [\mathcal{Q}(t)^T, \mathcal{P}(t)^T]^T$, $t \in [0, T]$.

As explained in Appendix A.1, for Hamiltonian dynamics Φ , *the left-hand side of the Fokker-Planck equation (5) is equal to the Poisson bracket between \mathcal{H} and p , i.e.*

$$\sum_{i=1}^D \frac{\partial}{\partial z_i} [\Phi_i(\mathbf{z}) p(\mathbf{z})] = \{\mathcal{H}, p\}(\mathbf{z}). \quad (7)$$

Consequently, when $p(\mathbf{z}) = \rho(\mathbf{z}) \propto \exp(-\mathcal{H}(\mathbf{z}))$, (7) vanishes as ρ is conserved (a first integral) under the Hamiltonian dynamics Φ . Thus under Hamiltonian deterministic dynamics, the only requirement for $\rho(\mathbf{z})$ being an invariant distribution is that (λ, Q) are chosen so that also the right-hand side of (5) also vanishes for $p(\mathbf{z}) = \rho(\mathbf{z})$.

3.1 Event specifications

Using the deterministic flow that preserves the target distribution afford substantial flexibility in choosing the two remaining ingredients, the event rate λ , and, at event transition distribution Q , which will collectively be denoted the “event specification”. This flexibility is very much in contrast to previous implementations of PDP-based Monte Carlo algorithms, based on constant or linear Φ , where the event rate is more or less fixed by the target distribution.

In this work, two “classes” of event specifications (λ, Q) are considered, with the necessary restriction that also the right-hand side of (5) vanishes when $p(\mathbf{z}) = \rho(\mathbf{z})$. These choices are by no means exhausting the possibilities, and only rather rudimentary but robust choices are considered here. Further research in this direction, in particular to obtain processes that have intervals between events well adapted to the target distribution similarly to e.g. the NUTS algorithm is currently being pursued.

3.1.1 Position-dependent event rates

The first class is, for some fixed $\phi \in (-1, 1)$, characterized by

$$\lambda(\mathbf{z}) = \omega(\mathbf{q}) > 0, \quad Q(\mathbf{z}|\mathbf{z}') = \delta(\mathbf{q} - \mathbf{q}')\mathcal{N}(\mathbf{p}|\phi\mathbf{p}', \sqrt{1 - \phi^2}\mathbf{M}). \quad (8)$$

I.e. in this case the event rate λ is only allowed to depend on the position variable \mathbf{p} , and $\delta(\cdot)$ is a Dirac delta function centered in $\mathbf{0}$. The autoregressive update constituting the \mathbf{p} -marginal of Q preserves the $(N(\mathbf{0}_d, \mathbf{M}))$ \mathbf{p} -marginal of ρ , whereas Q does not modify the position coordinate. Rather straight forward calculations detailed in Appendix A.2 show that also the right-hand side of (5) vanishes under the partial momentum refresh specification (8).

3.1.2 Momentum-dependent event rates

The second considered class of event specifications involves a more general $\lambda(\mathbf{z}) = \lambda(\mathbf{q}, \mathbf{p})$ only subject to $\lambda(\mathbf{z}) \geq 0$ and that $C(\mathbf{q}) = \int \lambda(\mathbf{q}, \mathbf{p})\mathcal{N}(\mathbf{p}|\mathbf{0}_d, \mathbf{M})d\mathbf{p} < \infty$ for all admissible \mathbf{q} . In this case, as detailed in Appendix A.3, choosing

$$Q(\mathbf{z}|\mathbf{z}') = \delta(\mathbf{q} - \mathbf{q}')\frac{\lambda(\mathbf{q}', \mathbf{p})\mathcal{N}(\mathbf{p}|\mathbf{0}, \mathbf{M})}{C(\mathbf{q}')} \quad (9)$$

also results in that the right-hand side of (5) vanishes. Similar choices of Q are discussed by Fearnhead et al. (2018, Section 3.2.1) and Vanetti et al. (2017, Section 2.3.3). Notice that allowing the event rate to depend on the momentum requires that the momentum refresh distribution must be modified relative to the Boltzmann distribution \mathbf{p} -marginal, and in practice the applicability of the approach is limited choices of λ

Event specification	λ	$Q(\mathbf{p} \mathbf{z}')$	Interpretation
1	$\frac{1}{\beta}$	$\mathcal{N}(\mathbf{p} \mathbf{0}_d, \mathbf{M})$	Time between events is $Exp(\beta)$, independent momentum refreshes
2	$\frac{1}{\beta}$	$\mathcal{N}(\mathbf{p} \phi\mathbf{p}', \sqrt{1-\phi^2}\mathbf{M}), \phi \in (-1, 1)$	Time between events is $Exp(\beta)$, autocorrelated momentum refreshes
3	$\frac{1}{\beta}\sqrt{\mathbf{p}^T\mathbf{M}^{-1}\mathbf{p}}$	$\propto \sqrt{\mathbf{p}^T\mathbf{M}^{-1}\mathbf{p}} \exp(-\frac{1}{2}\mathbf{p}^T\mathbf{M}^{-1}\mathbf{p})$	Arc-length of between-events (standardized) position trajectory is $Exp(\beta)$, independent momentum refreshes

Table 1: The event specifications applied in the remainder of this text. In all cases β is a tuning parameter, where larger β s on average correspond to less frequent events/longer inter-event trajectories. For specification 3, arc-lengths of position-trajectories are calculated in the Mahalanobis distance $d(\mathbf{q}, \mathbf{q}') = \sqrt{(\mathbf{q} - \mathbf{q}')^T \mathbf{M} (\mathbf{q} - \mathbf{q}')}$ as \mathbf{M}^{-1} is assumed to be some approximation/reflect the scales of the covariance matrix of $\pi(\mathbf{q})$.

so that $Q(\mathbf{p}|\mathbf{z}') \propto \lambda(\mathbf{q}', \mathbf{p})\mathcal{N}(\mathbf{p}|\mathbf{0}, \mathbf{M})$ allows efficient sampling. Examples of such cases include:

- λ allows the representation $\lambda(\mathbf{z}) = b(\mathbf{q}, \mathbf{p}^T \mathbf{M}^{-1} \mathbf{p})$ for suitably chosen function $b : \mathbb{R}^d \times \mathbb{R}^+ \mapsto \mathbb{R}^+$. Then, $Q(\mathbf{p}|\mathbf{z}')$ is an elliptically contoured distribution (see e.g. Cambanis et al., 1981) which typically allows efficient sampling.
- $\log(\lambda(\mathbf{z}))$ is a quadratic function in \mathbf{p} for each \mathbf{q} . Then $Q(\mathbf{p}|\mathbf{z}')$ is also Gaussian.

3.1.3 Specific event specifications

Table 1 provides the specific event specifications used in the remainder of this text. The former two are of type (8) whereas specification 3 is of type (9) with elliptically contoured momentum refresh distribution.

Specifications 1 and 2 lead to processes that have similarities to the Randomized HMC (RHMC) of Bou-Rabee and Sanz-Serna (2017). RHMC essentially reduces to an implementation of the hypothetical HMC-algorithm of section 2.2 based on symplectic integrators (and corresponding accept/reject steps) and exponentially distributed time increments s . The difference lies in that such an implementation of RHMC would sample the state of the process only at what would correspond to the event-times in the PDP formulation, whereas the PDP formulation allows the exploitation of the inter-event trajectories.

Interestingly, the large λ limit of the \mathbf{q} -component of the PDP, i.e. $\mathcal{Q}(t)$, for specification 1, is the Brownian motion-driven preconditioned Langevin process (see e.g. Roberts and Rosenthal, 1998) (see Appendix A.5)

$$d\mathcal{Q}(t) = \frac{1}{2}\mathbf{M}^{-1}\nabla_{\mathbf{q}}\log\tilde{\pi}(\mathcal{Q}(t)) + \mathbf{M}^{-\frac{1}{2}}d\mathbf{W}(t). \quad (10)$$

Here $\mathbf{W}(t)$ is a standard Brownian motion and $\mathbf{M}^{-\frac{1}{2}}$ is any matrix square-root of \mathbf{M}^{-1} .

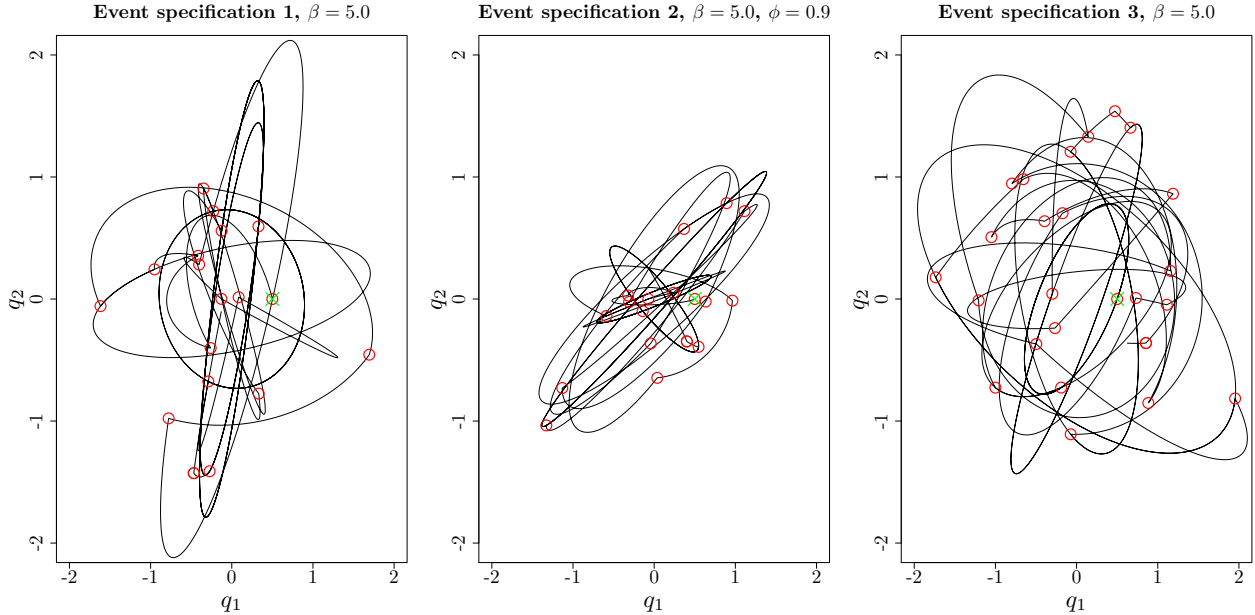


Figure 2: Examples of \mathbf{q} -coordinate of continuous time HMC trajectories with different event specifications for a bivariate standard Gaussian target distribution $\pi(\mathbf{q})$. In all cases, $\mathbf{M} = \mathbf{I}_2$ and the shown trajectories correspond 100 units of time t . Events are indicated with red circles, and the common initial \mathbf{q} -coordinate is indicated with a cross.

Specification 3 is a first attempt at providing event rates where the length of the between-event trajectories is chosen dynamically. Specifically, the event specification is chosen so that $\beta \int_0^v \lambda(\varphi_s(\mathbf{z})) ds = \beta \Lambda(v; \mathbf{z})$ is exactly the arc-length (in the Mahalanobis distance $d(\mathbf{q}, \mathbf{q}') = \sqrt{(\mathbf{q} - \mathbf{q}')^T \mathbf{M} (\mathbf{q} - \mathbf{q}')}$ for standardization, see Appendix Section A.6 for details) of the position coordinate when \mathbf{z} was the state of the process immediately after the last event. For this specification, $Q(\mathbf{p}|\mathbf{z}')$ allows straight forward sampling as it is an elliptically contoured distribution.

3.2 Illustrative examples

Figure 2 shows examples of the trajectories of the \mathbf{q} -coordinate under continuous time HMC process for different event specifications for a bivariate standard Gaussian target. It is seen that the nature of the trajectories differs, with event specification 2 visiting a rather narrow range of energy level sets. For event specification 1, there is quite large variation in the “how much ground” each between-event trajectory is covering (several of the between-event trajectories go through multiple identical cycles), whereas the arc-lengths have less variation under specification 3. Recall still that arc-lengths are only in expectation equal under event specification 3 as u appearing in (4) are exponentially distributed. From now on, only event specifications 1 and 3 are considered.

To gain some initial insight into the behavior of the CTHMC process for estimating the mean of a given

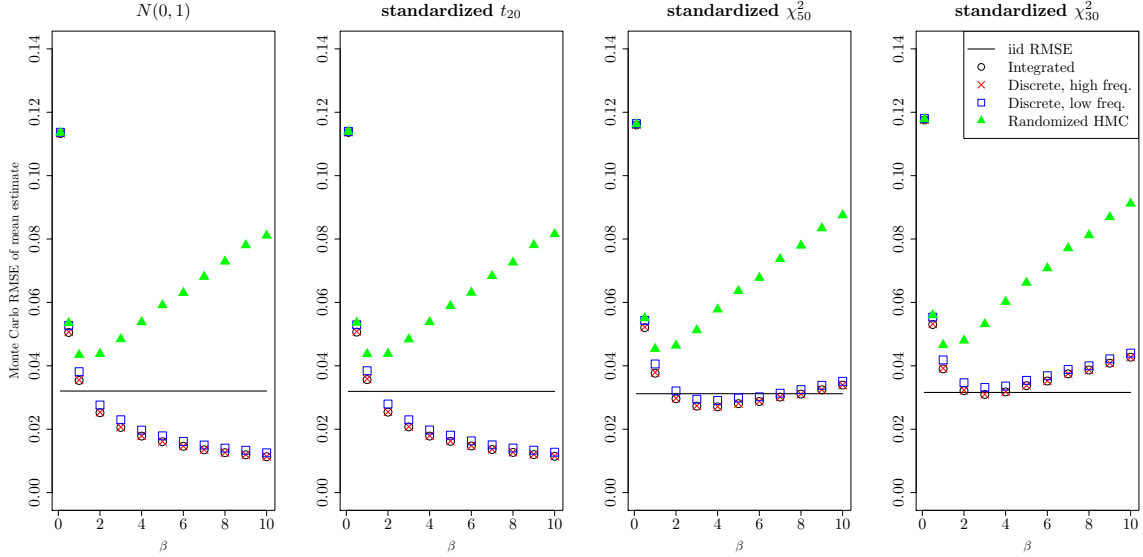


Figure 3: RMSE of estimates of $E(\mathbf{q}_1)$ from CTHMC processes using event specification 1 for different values of the mean inter-event time parameter β . The panels correspond to the different univariate target distributions $\pi(\mathbf{q}_1)$, which all have zero mean and unit variance. Unit mass matrix $M = 1$ was used. The estimates of the mean are based on trajectories of length $T = 1000\frac{\pi}{2}$, and the RMSE estimates are based on 10000 independent replica for each value of β . Black circles correspond continuous sampling (6), red \times -s to 1000 equally spaced samples, blue squares to 500 equally spaced samples and green triangles to randomized HMC. The horizontal lines give the RMSE of 1000 iid samples. The results are obtained using the numerical methods described in Section 4.1 with $tol_a = tol_r = 0.001$.

target, 10000 trajectories of were generated for 4 zero mean, unit variance univariate targets $\pi(\mathbf{q}_1)$. Each trajectory was of (time) length $T = 1000\frac{\pi}{2}$ preceded by an equal length of warmup. Event specification 1 was used in all cases, and experiments were repeated for different values of the inter-event mean time β (see Table 1). Further, several different sampling strategies were applied to all produced trajectories. Root mean squared errors (RMSEs) of the $E(\mathbf{q}_1)$ -estimates are presented in Figure 3.

For the standard Gaussian distribution, exactly iid samples obtains when choosing trajectories of (time) length $\pi/2$ in the hypothetical HMC method (Section 2.2). Thus, the (time) lengths of generated Hamiltonian flow (and thus essentially the computational cost) of CTHMC and for 1000 iid-samples-producing hypothetical HMC transitions are the same. As a reference to the CTHMC results, the RMSEs based on 1000 iid samples are also indicated as horizontal lines in the plots. For the non-Gaussian targets, the cost of obtaining RMSEs corresponding to 1000 iid samples using HMC are likely somewhat higher, and thus the benchmarks are likely somewhat favoring HMC in a computational cost perspective in these cases.

In all cases, low values of β (frequent events) result in poor results, as the continuous time process approaches the Langevin limit (10). The most striking feature of the plot is that for continuous (black circles) or high frequency sampling (red \times) of the trajectories, RMSEs for the symmetric targets ($N(0,1)$,

standardized t_{20}) decreases monotonically in β , and for the highest $\beta = 10.0$ considered is only around 35 percent of the benchmark in the $N(0, 1)$ case. In the univariate Gaussian target case, this behavior obtains as the between-event Hamiltonian dynamics, $\mathbf{q}_1(t)$, averaged over time, i.e. $\frac{1}{t} \int_0^t \mathbf{q}_1(s) ds$, converges to the mean of the target as $t \rightarrow \infty$, *regardless of the initial configuration $\mathbf{z}(0)$* (see below and Appendix B). Thus, in the Gaussian case, momentum refreshes are not necessary for unbiased estimation of $E(\mathbf{q}_1)$. It appears this is also the case for the standardized t_{20} -distribution, but this has not been proved formally so far.

For the non-symmetric targets, standardized χ_{50}^2 and standardized χ_{30}^2 , such monotonous behavior is not seen as momentum refreshes are certainly necessary in order to obtain high quality estimates. Too infrequent refreshes (i.e. high β) result in higher variance from exploring too few energy level sets. For intermediate values of β , the continuous- or high frequency sampling estimates are still better than or on par with the iid benchmark, where the edge is lost towards more skewness in the target distribution.

As mentioned in Section 2.3, the continuous time trajectories can either be sampled at discrete times or integrated over time as in (6). From Figure 3, it is evident that there is little difference in the high frequency ($\Delta = \pi/2$) sampling and continuous sampling. The efficiency deteriorates somewhat with more infrequent ($\Delta = \pi$) sampling (blue \square). As will be clear in the next section, integration-based estimates (6) require minimal additional numerical effort, and it seems advisable always to use these for moment calculations, whereas rather frequent samples should be used for other tasks.

The green triangles represent results obtained when sampling the process only at event times. Since the event rate is constant, this corresponds to the Randomized HMC (Bou-Rabee and Sanz-Serna, 2017, modulus leap frog integration) using the same amount of Hamiltonian trajectory. It is seen that this method, which does not exploit the “between-events” trajectories, generally lead to inferior results relative to CTHMC. The exception is in the random walk-like domain, where frequent sampling occurs also under the Randomized HMC, but in this case the underlying process only slowly explores the target distribution.

3.3 Choosing event intensities

The time average property under the univariate Gaussian, illustrated in the left panel of Figure 3 generalizes to multivariate Gaussian targets $\pi(\mathbf{q}) = \mathcal{N}(\mathbf{q}|\mu, \Sigma)$ as well. Namely, it can be shown (see Appendix B) that the between-events dynamics $\mathbf{q}(\tau)$ admit unbiased estimation of μ without momentum refreshes, i.e.

$$\frac{1}{T} \int_0^T \mathbf{C} \mathbf{q}(\tau) d\tau \xrightarrow{T \rightarrow \infty} \mathbf{C} \mu, \quad \mathbf{C} \in \mathbb{R}^{p \times d}, \quad (11)$$

regardless of the initial configuration $\mathbf{z}(0)$.

Of course, the Gaussian case in itself is not particularly interesting. However, one would presume that

for near Gaussian target distributions (which is frequently the case in Bayesian analysis applications due to central limit effects), the left-hand side (11) would have only a small variation in $\mathbf{z}(0)$ for large T . Hence such situations would benefit from quite low event intensities/long durations between events and would allow for very small Monte Carlo variations in moment estimates akin to those shown in the two leftmost panels of Figure 3 even in high-dimensional applications.

Still, the fast convergence results above are restricted to certain moments of certain target distributions. It is instructive (and sobering) to look at the estimation of the second order moment of a univariate standard Gaussian target distribution (with $\mathbf{M} = 1$). In this case,

$$\frac{1}{T} \int_0^T \mathbf{q}_1^2(\tau) d\tau \xrightarrow{T \rightarrow \infty} \frac{1}{2} (\mathbf{q}_1^2(0) + \mathbf{p}_1^2(0)),$$

i.e. the dependence on the initial configuration $\mathbf{z}(0)$ does not vanish as the time between events grows, and the second order moment cannot be estimated reliably without momentum refreshes.

For a fixed budget of Hamiltonian trajectories, a non-Gaussian target and/or a non-linear moment, say $E(g(\mathbf{q}))$, and the event rate tradeoff will have at the endpoints:

- For “large β ”, variation in the CTHMC moment estimate is mainly due to variation between energy level sets, i.e. the variance of $\lim_{T \rightarrow \infty} \int_0^T g(\mathbf{q}(t)) dt$ as a function of the initial configuration $\mathbf{z}(0)$.
- For “small β ”, variation in the CTHMC moment estimate comes mainly from that the underlying process \mathcal{Z}_t reverts to a random walk-like behavior (Langevin-dynamics for constant event rate).

The location of the optimum between these extremes (see e.g. the two right-most panels in Figure 3) inherently depends both on the target distribution and the collection of moments, say $E(g_1(\mathbf{q})), \dots, E(g_m(\mathbf{q}))$, one is interested in. More automatic choices of event rate specifications will be explored in the numerical experiments discussed below.

4 Numerical implementation

The proposed methodology relies on quite accurate simulation of the Hamiltonian trajectories and associated functionals of the type (6). This section summarizes numerical implementation of these quantities based on Runge-Kutta-Nystöm (RKN) methods (see e.g. Hairer et al., 1993, Chapter II.14). The reader is referred to Hairer et al. 1993 for more background on general purpose ODE solvers.

In what follows, τ is used as the time index of the between-events Hamiltonian dynamics (as opposed to PDP process time t), and it is convention that τ is reset to zero immediately after each event. RKN methods

are particularly well suited for time-homogenous second order ODE systems on the form

$$\ddot{\mathbf{y}}(\tau) = \mathbf{F}(\mathbf{y}(\tau)), \mathbf{y} \in \mathbb{R}^n, \mathbf{F} : \mathbb{R}^n \mapsto \mathbb{R}^n, \quad (12)$$

subject to the initial conditions $\mathbf{y}(0) = \mathbf{y}_0, \dot{\mathbf{y}}(0) = \mathbf{z}_0$. Notice that when \mathbf{F} does not depend on $\dot{\mathbf{y}}(\tau)$, RKN methods are substantially more efficient than applying conventional Runge Kutta methods to an equivalent coupled system of $2n$ first order equations, say $\dot{\mathbf{y}}(\tau) = \mathbf{w}(\tau), \dot{\mathbf{w}}(\tau) = \mathbf{F}(\mathbf{y}(\tau))$.

A wide range of numerical methods have been developed specifically for the dynamics of Hamiltonian systems (see e.g. Sanz-Serna and Calvo, 1994; Leimkuhler and Reich, 2004). Such methods typically conserve the symplectic- and time-reversible properties of the true dynamics, and hence provide reliable long-term simulations over many (quasi-)orbits. However, for shorter time spans, typically on the order of up to a few (quasi-)orbits, such symplectic methods have no edge over conventional methods for second order ODEs (see e.g. Sanz-Serna and Calvo, 1994, Section 9.3).

4.1 Numerical solution of dynamics and functionals

In the numerical implementation used in the present work, the between-events Hamiltonian dynamics are reformulated in terms of the second order ODE

$$\ddot{\mathbf{q}}(\tau) = \mathbf{M}^{-1} \nabla_{\mathbf{q}} \log(\mathbf{q}(\tau)), \quad (13)$$

which is to be solved for $(\mathbf{q}(\tau), \dot{\mathbf{q}}(\tau))$. The dynamics of (13) are equivalent to the dynamics of (2) when the initial conditions $(\mathbf{q}(0), \dot{\mathbf{q}}(0) = \mathbf{M}^{-1} \mathbf{p}(0))$ are applied, and the momentum variable for any τ is recovered via $\mathbf{p}(\tau) = \mathbf{M} \dot{\mathbf{q}}(\tau)$.

Further, recall that the proposed methodology relies critically on the ability to calculate between-events Hamiltonian dynamics functionals on the form

$$\mathbf{r}_k(\tau) = \int_0^\tau \mathcal{M}_k(\mathbf{q}(s)) ds, \quad k = 1, \dots, p, \quad (14)$$

for a suitably chosen monitoring function $\mathcal{M} : \mathbb{R}^d \rightarrow \mathbb{R}^p$, e.g. for integrated event intensities Λ (4) and continuous sampling (6). To this end, first observe that $\mathbf{r}(\tau) = \dot{\mathbf{R}}(\tau)$ whenever $\ddot{\mathbf{R}}(\tau) = \mathcal{M}(\mathbf{q}(\tau))$, with initial

conditions $\mathbf{R}(0) = \mathbf{0}_p$, $\dot{\mathbf{R}}(0) = \mathbf{0}_p$. Hence by augmenting (13) with the monitoring function, i.e.

$$\begin{bmatrix} \ddot{\mathbf{q}}(\tau) \\ \ddot{\mathbf{R}}(\tau) \end{bmatrix} = \begin{bmatrix} \mathbf{M}^{-1} \nabla_{\mathbf{q}} \log(\mathbf{q}(\tau)) \\ \mathcal{M}(\mathbf{q}(\tau)) \end{bmatrix}, \quad (15)$$

a system on the form (12) is obtained. When solved numerically, (15) produces solutions both for the dynamics (2 or 13) and the dynamics functional (14). Implemented in this manner, the adaptive step size methodology (discussed in the Appendix) controls both the numerical error in the Hamiltonian dynamics and the functionals concurrently.

In this work, the 6th order explicit embedded pair RKN method RKN6(4)6FD of Dormand and Prince (1987, Table 2) was used to solve (15). Each step of RKN6(4)6FD requires 5 evaluations of the right-hand side of (15), but of course being a higher order method, the step sizes may typically be substantially larger than the stability limit of e.g. the leap frog method. Since the solution to $\mathbf{R}(\tau)$ is not required per se, trivial modifications of the mentioned RKN method were done so that it solves only for $\mathbf{s}(\tau) = (\mathbf{q}(\tau), \dot{\mathbf{q}}(\tau), \mathbf{r}(\tau))$. Further details, and a full algorithm may be found in Section C in the Appendix.

4.2 Do numerical errors influence results?

In order to assess how the application of (un-corrected) RKN numerical integrators for the Hamiltonian dynamics influences overall Monte Carlo estimation, a small simulation experiment was performed. Specifically, a $N(\mathbf{0}_2, \Sigma)$ target distribution with

$$\Sigma = \begin{bmatrix} 1 & 2 \\ 2 & 8 \end{bmatrix}, \quad \mathbf{M} = \mathbf{I}_2, \quad \lambda = \frac{1}{10} \quad \text{and} \quad Q(\mathbf{p}|\mathbf{z}') = \mathcal{N}(\mathbf{p}|\mathbf{0}_2, \mathbf{M}), \quad (16)$$

was used. Due to the Gaussian nature of the target distribution, the Hamiltonian dynamics are available in closed form, and hence allow the comparison with the numerically integrated counterparts. CTHMC trajectories based both on exact and numerically integrated dynamics were used to estimate the mean and raw second order moments of the target using continuous sampling. The same initial configuration $\mathcal{Z}(0)$ and the same random numbers were used so that errors in the estimators based on numerical integration are due only to RKN integration. Figure 4 shows the RMSEs between estimates from numerically integrated- and exact CTHMC trajectory for different values of T and the absolute (relative) RKN integrator error tolerance tol_a (tol_r). All results are based on independent 50 replications. Also indicated in the plots as horizontal lines are the RMSEs associated with estimating the said moments (across multiple independent trajectories) based on CTHMC with exact dynamics.

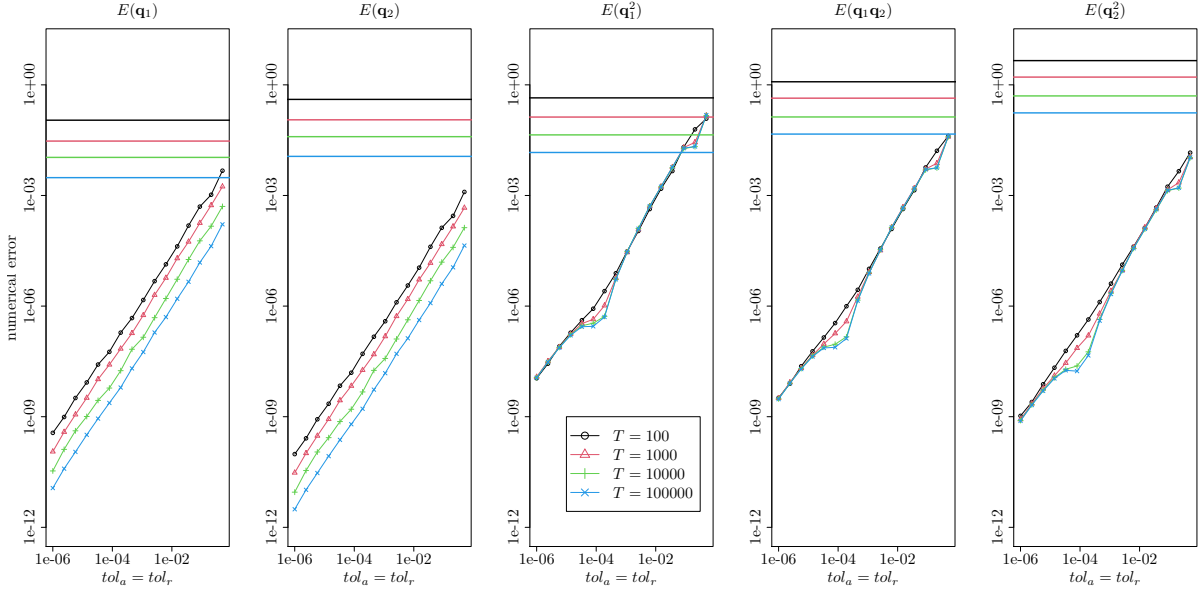


Figure 4: Numerical errors incurred by RKN integration on the estimation the first and second order moments of a bivariate Gaussian target distribution. The numerical errors are relative to a CTHMC trajectory using the same random numbers but with exact Hamiltonian dynamics. Both exact and numerically integrated results are based on continuous sampling. The horizontal axis gives the error tolerances (in all cases with $tol_a = tol_r$) applied in the numerical integrator, and both horizontal and vertical axis are logarithmic. Dotted lines indicate the root mean squared errors associated with estimating given the moments across many exact CTHMC trajectories of different length T .

From Figure 4, it is seen that except for very large values of $tol_a = tol_r$, the numerical errors are very small relative to the exact estimator RMSEs. From the plots, absolute and relative error tolerances of around 0.001 appear to be more than sufficient for this case. Interestingly, it is seen that there is no apparent buildup of numerical errors of in the longer trajectories, suggesting that the incurred errors are not systematically accumulating and biasing the estimation in any direction. Of course, this limited experiment does not rule out such biasing behavior in general. However, the overall the finding here indicate that quite lax error tolerances are sufficient to make the numerical errors be negligible relative to overall Monte Carlo variation.

4.3 Automatic selection of tuning parameters

A key aim of developing CTHMC processes is to enable the implementation of an easy to use and general-purpose code. For this purpose, automatic selection of tuning parameters is important. This Section describes the routines for tuning the mass matrix \mathbf{M} and scaling the event intensity used in the computations described shortly.

4.3.1 Tuning of mass matrix

In the present work, only a diagonal mass matrix $\mathbf{M} = \text{diag}(m_1, \dots, m_d)$ is considered. Two approaches for choosing each of m_1, \dots, m_d are considered, both exploiting the ability to numerically calculate temporal averages by augmenting the monitoring function \mathcal{M} .

In former approach which will be referred to as VARI (variance, integrated), m_i^{-1} is simply set equal to the temporal average estimate of $\text{Var}(\mathbf{q}_i)$, i.e.

$$\int_0^{t^*} \mathcal{Q}_i^2(s) ds - \left[\int_0^{t^*} \mathcal{Q}_i(s) ds \right]^2,$$

at every event time t^* during the warmup period.

In cases where the marginal variances are less informative with respect to the local scaling of the target distribution, e.g. in the presence of strong non-linearities or multimodality, a second approach referred to as ISG (integrated squared gradients) may also be pursued. Here overarching idea for choosing each of m_1, \dots, m_d is to make the square of each element of the right-hand side of (13), averaged over *each integrator step*, in expectation over all integrator steps, to be equal to 1. This approach is mainly motivated out of numerical efficiency considerations, where regions of the target distribution requiring many steps (with short step sizes due to strong forces $\nabla_{\mathbf{q}} \log \tilde{\pi}(\mathbf{q})$) are disproportionately weighted when choosing the mass matrix.

More explicitly, let the j th integrator step (during the warmup period) be originating at time τ_j and have time step size ε_j . Then the mass matrix diagonal m_i is taken to be an exponential moving average (over j) of

$$\frac{1}{\varepsilon_j} \int_{\tau_j}^{\tau_j + \varepsilon_j} [\nabla_{\mathbf{q}} \log \tilde{\pi}(\mathbf{q}(s))]_i^2 ds.$$

Notice that the integrated squared gradients are available at negligible additional cost by augmenting \mathcal{M} in the ODE system (15) with moment functions $[\nabla_{\mathbf{q}} \log \tilde{\pi}(\mathbf{q})]_i^2$, $i = 1, \dots, d$. Further notice that for a $N(\mu, \mathbf{P}^{-1})$ target distribution, where $E_{\pi}([\nabla_{\mathbf{q}} \log \tilde{\pi}(\mathbf{q})][\nabla_{\mathbf{q}} \log \tilde{\pi}(\mathbf{q})]^T) = \mathbf{P}$, this approach may (modulus variability in integrator step size) be seen as a way to *directly estimate the precision matrix diagonal elements*.

4.3.2 Tuning of event rates

The methodology for tuning the event rates relies of the following representation of a general event rate λ :

$$\lambda(\mathbf{q}, \mathbf{p}) = \frac{1}{\gamma\beta} \bar{\lambda}(\mathbf{q}, \mathbf{p}), \quad \gamma > 0, \beta > 0,$$

where $\bar{\lambda}$ is a “base line” event rate (e.g. $\bar{\lambda} = 1$ for event specification 1 and 2, and $\bar{\lambda} = \sqrt{\mathbf{p}^T \mathbf{M}^{-1} \mathbf{p}}$ for event specification 3). Here γ is a user-given scale factor, say in the range 1 to 20, chosen in the higher range if one expects good performance with infrequent moment refreshes (see Section 3.3). Finally, β is tuned automatically to reflect each particular target distribution. The objective of the automatic event rate tuning is given by

$$E_{\mathbf{z}(0) \sim \rho(\mathbf{z})} \left(\frac{1}{\beta} \int_0^\omega \bar{\lambda}(\mathbf{q}(\tau), \mathbf{p}(\tau)) d\tau \right) = 1, \quad (17)$$

where ω is the “no-U-turn” time of the dynamics (Hoffman and Gelman, 2014)

$$\omega = \inf \{ \tau > 0 : (\mathbf{q}(\tau) - \mathbf{q}(0))^T \mathbf{p}(\tau) < 0 \},$$

(See also Wu et al., 2018, for a similar development). The rationale behind (17) is that (for $\gamma = 1$) the expected integrated event rate Λ (see Equation 4) evaluated at corresponding no-U-turn time is equal to $E(u)$.

In practice, realizations of $\int_0^\omega \bar{\lambda}(\mathbf{q}(\tau), \mathbf{p}(\tau)) d\tau$ are recorded for each between-events Hamiltonian trajectory during the warmup period (i.e. if events occur before the no-U-turn time, further integration steps are performed to find ω). Subsequently, β^{-1} set equal to an exponential moving average of these realizations.

5 Numerical experiments

This section considers numerical experiments and benchmarking of the proposed method against the current NUTS-HMC implementation in Stan (rstan version 2.21.2). Like Stan, the proposed methodology has been implemented as an R package (pdphmc) with main computational tasks done in C++, and relies on the Stan Math Library (Carpenter et al., 2017) for automatic differentiation and probability- and linear algebra computations. Consequently, CPU-times are directly comparable. All computations in this section were carried out on a 2020 Macbook pro with a 2.6 GHz Intel Core i7 processor, under R version XXX. Unless otherwise noted, the default integrator tolerances $tol_a = tol_r = 0.001$ are used for pdphmc. The package pdphmc, and code and data for reproducing the reported results is available at <https://github.com/torekleppe/PDPHMCpaperCode>.

In order to compare the performance of the methods, their Effective Sample Size (ESS) (Geyer, 1992) per computing time (see e.g. Girolami and Calderhead, 2011) is taken as the main statistic. Consider a sample dependent of dependent random variables η_i , $i = 1, \dots, N$, each having the same marginal distribution. The ESS gives the number of hypothetical iid samples (with distribution equal to that of η_1) required to obtain a mean estimator with the same variance as $N^{-1} \sum_{i=1}^N \eta_i$. An ESS-based approach is taken also here, but

	rstan, $\delta = 0.8$	rstan, $\delta = 0.9$	rstan, $\delta = 0.99$	rstan, $\delta = 0.999$	pdphmc
CPU time (s)	0.74	0.99	2.52	4.80	15.02
\mathbf{q}_1 ESS	1795	2132	1477	2245	11794
\mathbf{q}_1 ESS / CPU time	2421	2144	587	467	785

Table 2: Computing time and ESS for the funnel distribution $\mathbf{q}_1 \sim N(0, 1)$, $\mathbf{q}_2|\mathbf{q}_1 \sim N(0, \exp(3\mathbf{q}_1))$. Reported CPU time numbers are total sampling time (i.e. excluding warmup) across the 10 replica, and the reported ESSes are also the total ESS represented by the 50,000 samples (10 chains/trajectories times 5000 samples of each). Notice that the rstan methods struggle to explore the target distribution (see in Section 2.2 and Figure 1), and the numbers are therefore not directly comparable.

in order to obtain ESSes for moments estimated by for integrated quantities (6), the following approach was taken: For a given number of samples, say N , rewrite the left-hand side of (6) as

$$\frac{1}{T} \int_0^T g(\mathcal{Z}(t))dt = \frac{1}{N} \sum_{i=1}^N \eta_i, \text{ where } \eta_i = \Delta^{-1} \int_{(i-1)\Delta}^{i\Delta} g(\mathcal{Z}(t))dt, \Delta = \frac{T}{N}. \quad (18)$$

Let $\widehat{ESS}_i(\eta_i)$ denote an estimator of the ESS of dependent sample η_i . Then

$$\frac{\widehat{Var}_i(g(\mathcal{Z}(\Delta i)))}{\widehat{Var}_i(\eta_i)} \widehat{ESS}(\eta_i) \quad (19)$$

is taken to be an estimator of ESS represented by moment estimator $T^{-1} \int_0^T g(\mathcal{Z}(t))dt$. Equation 19 takes into account both that $\widehat{Var}_i(\eta_i)$ tends to be smaller than $\widehat{Var}_i(g(\mathcal{Z}(\Delta i)))$ due to the temporal averaging in (18), but on the other hand η_i tends to exhibit a stronger autocorrelation than discrete time samples $g(\mathcal{Z}(\Delta i))$. Throughout this text, the ESS estimation procedure in rstan (see R-function `rstan::monitor()`, output “n_eff”) was used for estimating ESS from samples.

In what follows, three numerical experiments are presented. A further experiment, a crossed random effects model for the Salamander data may be found in Section D of the Appendix. For the Salamander data, pdphmc is found to be on par or somewhat more efficient than rstan.

5.1 Funnel distribution

The Funnel distribution $\mathbf{q}_1 \sim N(0, 1)$, $\mathbf{q}_2|\mathbf{q}_1 \sim N(0, \exp(3\mathbf{q}_1))$ (funnell distributions may be traced back to Neal, 2003), constituting the first numerical example, has already been encountered in Section 2.2 and Figure 1. This very simple example may be considered as a “model problem” displaying similar behavior as for targets associated with Bayesian hierarchical models (where q_1 plays the role of latent field log-scale parameter, and q_2 plays the role of the latent field it self).

Both rstan and pdphmc uses identity mass matrices. Except for the target acceptance rate δ and mass

matrix, the remaining tuning parameters of rstan are the default. Both for rstan and pdphmc, 10 independent chains/trajectories were run. For rstan, each of these chains had 10,000 transitions with 5,000 discarded as warmup. Note that rstan outputs a substantial number of warnings related to diverged transitions.

For pdphmc, the trajectories were of length $T = 100,000$, sampled discretely $N = 10,000$ times and with the former half of samples discarded as warmup. For such high sampling frequency, continuous samples yield similar results as the discrete samples, and are thus not discussed further here. A constant event rate $\lambda = \beta^{-1}$ was applied, and β was adapted with scale factor $\gamma = 2$ using the methodology described in Section 4.3.2. The adaptive selection resulted in values of β between 2.1 and 4.7 across the 10 trajectories, which again translates to between 0.21 and 0.48 discrete time samples per (between-events) Hamiltonian trajectory.

It has already been visually confirmed from Figure 1 that the output of rstan does not fully explore the target distribution. Still, it is instructive to study the relative performance for sampling the log-scale parameter \mathbf{q}_1 across the different methods. Table 2 presents CPU times and the ESS of \mathbf{q}_1 . It is seen that pdphmc requires somewhat more CPU time per effective sample for the (visibly defective) rstan runs with the lowest fidelity leap frog integration. Moreover, pdphmc has a better sampling performance than (marginally converged) rstan, $\delta = 0.999$. In sum, these observations give indication that the proposed methodology may have substantial edge against conventional NUTS-HMC sampling for difficult target distributions, even before more adaptive event intensities have been considered.

5.2 Smile-shaped distribution

To further explore the performance of pdphmc applied to a highly non-linear target distributions; the “smile”-shaped distribution

$$\mathbf{q}_k | \mathbf{q}_1 \sim N(\mathbf{q}_1^2, 0.5^2), \quad k = 2, \dots, 11, \quad (20)$$

$$\mathbf{q}_1 \sim N(0, 1). \quad (21)$$

is considered. The results for various settings of pdphmc and rstan are given in Table 3. From the Table, it is seen that rstan has substantial convergence problems, whereas the various settings of pdphmc reliably explores the target. Choosing longer trajectories ($\gamma = 10$) results in higher sampling efficiency for the marginally standard Gaussian \mathbf{q}_1 , whereas for the non-Gaussian components $\mathbf{q}_{2:11}$, shorter trajectories are more efficient. Comparing the event specifications 1 and 3, it is seen that none of them produces uniformly better results.

γ	sampling	\mathbf{q}_1		$\min_{k \in (2,11)} ESS(\mathbf{q}_k)$		$\max_{k \in (2,11)} ESS(\mathbf{q}_k)$		$E(\mathbf{q}_1)$	$E(\mathbf{q}_2)$	CPU time
		ESS	$\frac{ESS}{CPU\ time}$	ESS	$\frac{ESS}{CPU\ time}$	ESS	$\frac{ESS}{CPU\ time}$	(exact = 0)	(exact = 1)	(s)
rstan										
		19	10	29	15	32	17	-0.15	1.04	1.9
pdphmc, event specification 1 (see Table 1)										
2	D	1323	779	1065	627	1215	716	-0.02	1.03	1.7
2	C	1319	777	1115	657	1150	678	-0.02	1.02	
10	D	2213	1304	608	358	634	374	0.01	1.00	1.7
10	C	2233	1316	613	361	630	371	0.01	1.01	
pdphmc, event specification 3 (see Table 1)										
2	D	1094	645	1130	666	1183	697	-0.02	0.98	1.7
2	C	1094	645	1153	679	1184	698	-0.02	0.97	
10	D	2276	1341	920	542	967	570	0.01	1.03	1.7
10	C	2303	1357	927	546	948	559	0.01	1.03	

Table 3: Results for the “smile”-shaped target distribution (20,21). The results are based on 10 independent replica, and ESSes and ESSes per computing time (best in bold font) are from the combined results over these replica. For rstan, each replica consists of the 10,000 transitions, with the former 5,000 discarded as warmup. For pdphmc, ISG-type mass matrix, trajectories of length $T = 25,000$ divided evenly between warmup and sampling, and 1000 discrete samples were used. The presented CPU times are the total time spent by all chains/trajectories during the post warmup period. For each configuration of pdphmc, results from both discrete sampling (D) and continuous sampling (C) are presented.

5.3 Logistic regression

The next example model is a basic logistic regression model

$$\mathbf{y}_i | \boldsymbol{\beta} \sim \text{Beroulli}(\mathbf{p}_i), \text{logit}(\mathbf{p}_i) = \mathbf{x}_i^T \boldsymbol{\beta}, i = 1, \dots, n, \quad (22)$$

$$\boldsymbol{\beta} \sim N(\mathbf{0}_p, 100\mathbf{I}_p) \quad (23)$$

applied to the German credit data (see e.g. Michie et al., 1994) which has $n = 1000$ examples and $p = 25$ covariates (including a constant term). This example is included to measure the performance relative to rstan on an “easy” target distribution (Chopin and Ridgway, 2017).

Results for pdphmc and rstan are provided in Table 4. It is seen that rstan produces less variation in the ESSes across the different parameters than pdphmc, which presumably is related to the mass matrix adaptation. The discrete samples cases of pdphmc have a somewhat slower minimum ESS performance but on par or better median- and maximum ESS performance. For this target distribution, continuous samples for the first moment of $\boldsymbol{\beta} | \mathbf{y}$ substantially improves the performance of pdphmc relative to the corresponding discretely sampled counterparts in all cases.

γ	Sampling	$\min_j \widehat{ESS}(\beta_j)$		$\text{median}_j \widehat{ESS}(\beta_j)$		$\max_j \widehat{ESS}(\beta_j)$		CPU time
		ESS	$\frac{\text{ESS}}{\text{CPU time}}$	ESS	$\frac{\text{ESS}}{\text{CPU time}}$	ESS	$\frac{\text{ESS}}{\text{CPU time}}$	
rstan								
		9676	2125	13450	2953	15812	3472	4.55
pdphmc, event specification 1								
5	D	11350	1425	23114	2903	40000	5023	7.96
5	C	18220	2288	32967	4140	71079	8926	
20	D	11853	1490	29752	3740	40000	5028	7.96
20	C	20423	2567	36019	4528	69623	8752	
pdphmc, event specification 3								
5	D	11281	1362	23185	2799	40000	4829	8.28
5	C	18317	2211	30771	3715	66928	8080	
20	D	12780	1565	32653	3999	40000	4899	8.16
20	C	20902	2560	43303	5304	70584	8645	

Table 4: ESSes and time weighted ESSes for the logistic regression model (22,23) applied to the German credit data. All figures are based on 10 independent chains/trajectories. For rstan, the default 1000 warmup transitions followed by 1000 sampling transitions were used. For pdphmc, a VARI mass matrix, $T = 5000$ divided evenly between warmup and sampling and 1000 discrete samples per trajectory were used.

6 Dynamic Inverted Wishart model for realized covariances

6.1 Model and data

As a large scale illustrative application of CTHMC, the dynamic inverted Wishart model for realized covariance matrices (Golosnoy et al., 2012) of Grothe et al. (2019) is considered. Under this model, a time series of SPD covariance matrices $\mathbf{Y}_k \in \mathbb{R}^{G \times G}$, $k = 1, \dots, n$ are modeled independently inverted Wishart distributed conditionally on a latent time-varying SPD scale matrix Σ_k and a degree of freedom parameter $\nu > G + 1$, i.e.

$$\mathbf{Y}_k | \Sigma_k, \nu \sim \text{inv-Wishart}(\nu, \Sigma_k) \quad (24)$$

so that $E(\mathbf{Y}_k | \Sigma_k, \nu) = (\nu - G - 1)^{-1} \Sigma_k$. The time-varying scale matrix is in turn specified in terms of

$$\Sigma_k = \mathbf{H}[\text{diag}(\exp(\mathbf{x}_{1,k}), \dots, \exp(\mathbf{x}_{G,k}))]\mathbf{H}^T \quad (25)$$

where $\mathbf{H} \in \mathbb{R}^{G \times G}$ is a lower triangular matrix with $\mathbf{H}_{g,g} = 1$, $g = 1, \dots, G$. The remaining (strictly lower triangular) elements $\mathbf{H}_{i,j}$, $j = 1, \dots, G - 1, i = j + 1, \dots, G$, are unrestricted parameters. Finally, the log-scale factors $\mathbf{x}_{g,k}$ are a-priori independent (over g) stationary Gaussian AR(1) processes

$$\mathbf{x}_{g,k} = \boldsymbol{\mu}_g + \boldsymbol{\delta}_g(\mathbf{x}_{g,k-1} - \boldsymbol{\mu}_g) + \boldsymbol{\sigma}_g \varepsilon_{g,k}, \quad \varepsilon_{g,k} \sim \text{iid } N(0, 1), \quad k = 2, \dots, n, \quad g = 1, \dots, G, \quad (26)$$

$$\mathbf{x}_{g,1} \sim N(\boldsymbol{\mu}_g, \boldsymbol{\sigma}_g^2 / (1 - \boldsymbol{\delta}_g^2)), \quad g = 1, \dots, G, \quad (27)$$

		rstan	pdphmc, event spec. 1, $\gamma = 10.0$		pdphmc, event spec. 3, $\gamma = 10.0$	
CPU time (S,A)		(14605, 72127)	(10629, 25244)		(10189, 24960)	
sampling			D	C	D	C
μ	ESS (min, max)	(14304, 18487)	(12906, 28173)	(14467, 28370)	(14749, 38387)	(14224, 41821)
	ESS/S (min, max)	(0.98, 1.27)	(1.21, 2.65)	(1.36, 2.67)	(1.45, 3.77)	(1.40, 4.10)
	ESS/A (min, max)	(0.20, 0.26)	(0.51, 1.12)	(0.57, 1.12)	(0.59, 1.54)	(0.57, 1.68)
σ	ESS (min, max)	(14757, 20011)	(28447, 38922)	(35971, 42891)	(30227, 40000)	(34283, 44316)
	ESS/S (min, max)	(1.01, 1.37)	(2.68, 3.66)	(3.38, 4.04)	(2.97, 3.93)	(3.36, 4.35)
	ESS/A (min, max)	(0.20, 0.28)	(1.13, 1.54)	(1.42, 1.70)	(1.21, 1.60)	(1.37, 1.78)
δ	ESS (min, max)	(13624, 16678)	(16145, 28401)	(18109, 31180)	(15749, 25582)	(9464, 29271)
	ESS/S (min, max)	(0.93, 1.14)	(1.52, 2.67)	(1.70, 2.93)	(1.55, 2.51)	(0.93, 2.87)
	ESS/A (min, max)	(0.19, 0.23)	(0.64, 1.13)	(0.72, 1.24)	(0.63, 1.02)	(0.38, 1.17)
\mathbf{H}	ESS (min, max)	(12195, 22072)	(35292, 40000)	(46273, 69861)	(33089, 40000)	(43658, 70275)
	ESS/S (min, max)	(0.84, 1.51)	(3.32, 3.76)	(4.35, 6.57)	(3.25, 3.93)	(4.28, 6.90)
	ESS/A (min, max)	(0.17, 0.31)	(1.40, 1.58)	(1.83, 2.77)	(1.33, 1.60)	(1.75, 2.82)
ν	ESS	17797	40000	53388	40000	56313
	ESS/S	1.22	3.76	5.02	3.93	5.53
	ESS/A	0.25	1.58	2.11	1.60	2.26
$\mathbf{z}_{1,\cdot}$	ESS (min, max)	(22130, 24317)	(30533, 40000)	(37065, 70920)	(40000, 40000)	(64787, 68952)
	ESS/S (min, max)	(1.52, 1.67)	(2.87, 3.76)	(3.49, 6.67)	(3.93, 3.93)	(6.36, 6.77)
	ESS/A (min, max)	(0.31, 0.34)	(1.21, 1.58)	(1.47, 2.81)	(1.60, 1.60)	(2.60, 2.76)
$\mathbf{x}_{1,\cdot}$	ESS (min, max)	(22149, 24858)	(27525, 40000)	(33768, 70763)	(40000, 40000)	(63230, 68873)
	ESS/S (min, max)	(1.52, 1.70)	(2.59, 3.76)	(3.18, 6.66)	(3.93, 3.93)	(6.21, 6.76)
	ESS/A (min, max)	(0.31, 0.34)	(1.09, 1.58)	(1.34, 2.80)	(1.60, 1.60)	(2.53, 2.76)

Table 5: Effective sample sizes and computing times for the dynamic inverted Wishart model (24,27). In all cases, the results are based on 10 independent chains/trajectories and reported computing times are the total computing times over these 10 replica. For rstan, default sampler parameters with 1000 warmup transitions followed by 1000 sampling transitions were used. For pdphmc, $T = 5000$ split evenly between warmup and sampling, 1000 samples and an VARI type diagonal mass matrix were applied. Both computing times for the sampling (S) period and for all (A) computations (warmup and sampling) are provided, and ESSes are weighted both for S and A.

where $\boldsymbol{\mu}_g, \boldsymbol{\delta}_g \in (-1, 1), \boldsymbol{\sigma}_g > 0, g = 1, \dots, G$ are parameters.

The joint distribution of parameters $\boldsymbol{\theta} = (\boldsymbol{\mu}, \boldsymbol{\delta}, \boldsymbol{\sigma}, \mathbf{H}_{2:G,1}, \dots, \mathbf{H}_{G,G-1}, \nu)$ and latent variables \mathbf{x} is difficult to sample from, and in order to reduce “funnel” effects, the Laplace-based transport map reformulation of Osmundsen et al. (2019) (without Newton iterations) is used here. For every admissible $\boldsymbol{\theta}$, a smooth bijective mapping, say $\mathbf{x} = \gamma_{\boldsymbol{\theta}}(\mathbf{z}), \mathbf{z} \in \mathbb{R}^{Gn}$, is introduced so that $p(\mathbf{z}, \boldsymbol{\theta} | \mathbf{Y}_{1:n}) \propto |\nabla_{\mathbf{z}} \text{vec}(\gamma_{\boldsymbol{\theta}}(\mathbf{z}))| [p(\mathbf{x}, \boldsymbol{\theta} | \mathbf{Y}_{1:n})]_{\mathbf{x}=\gamma_{\boldsymbol{\theta}}(\mathbf{z})}$ approximates $p(\boldsymbol{\theta} | \mathbf{Y}_{1:n}) \mathcal{N}(\mathbf{z} | \mathbf{0}_{Gn}, \mathbf{I}_{Gn})$. Subsequently, CTHMC/HMC targeting $p(\mathbf{z}, \boldsymbol{\theta} | \mathbf{Y}_{1:n})$ are performed. The reader is referred Appendix E and Osmundsen et al. (2019) for more details on the construction of $\gamma_{\boldsymbol{\theta}}$ and also Appendix E for further details such as priors.

The data considered are $n = 2514$ daily observations of realized covariance matrices for $G = 5$ stocks (American Express, Citigroup, General Electric, Home Depot, IBM) between January 1, 2000 and December 31, 2009. See Golosnoy et al. (2012) for details on how this dataset was constructed from high frequency financial data. For these values of n and G , the model involves $Gn = 12570$ latent variables and $3G + G(G - 1)/2 + 1 = 26$ parameters.

6.2 Results

ESSes and time-weighted ESSes for the parameters, $\mathbf{z}_{1:5,1}$ and $\mathbf{x}_{1:5,1}$ are given in Table 5 for two variants of pdphmc and an rstan benchmark. It is seen that the discretely sampled (D) pdphmc uniformly provides faster sampling performance than rstan. The speedup is in particularly significant when taking all (A) computations into account as rstan uses more than 80% of the computing time in the warmup phase, whereas there is relatively little warmup overhead for pdphmc. For continuously sampled (C) pdphmc the picture is somewhat more mixed with numbers ranging from being on par with rstan ($\boldsymbol{\delta}$, event specification 3) to being up to five times faster (\mathbf{H} , both event specifications). Event specification 3 lead to better worst case performance than event specification 1 in all cases other than for \mathbf{H} . However the differences are not very large. Still this observation suggest that it may be possible to gain even more efficiency by developing more adaptive event rate specifications.

Posterior means and standard deviations obtained both from rstan and discretely sampled pdphmc presented in Table 7 in the Appendix show no noteworthy deviations (see also Grothe et al., 2019, Table 5). To conclude, pdphmc is fast and reliable alternative to HMC that also scale well to high-dimensional settings.

7 Discussion

This paper has introduced continuous time Hamiltonian Monte Carlo processes as a new, robust and potentially very efficient alternative to conventional MCMC methods. The presently proposed methodology

holds promise to be substantially more trustworthy for complicated real-life problems. This improvement is related to two factors:

- The CTHMC process is time-irreversible, and the present paper is to the author’s knowledge the first attempt to leverage time-irreversible processes to produce general purpose and easy to use MCMC-like samplers that scale to high-dimensional problems. By now, there is substantial evidence (see e.g. discussion on page 387 of Fearnhead et al., 2018) that irreversible processes are superior to conventional reversible alternatives such as HMC. In particular, irreversible methods appear to be more robust to irregular target distributions, as transition can be made without regard to the likelihood of the corresponding reversed transition occurring.
- The proposed implementation of CTHMC process leverages the mature, and widely used field of numerical integration of ordinary differential equations. Common practice for HMC is choosing a fixed step size low order symplectic method and hoping that regions where this step size is too large for numerical stability is not encountered during the simulation. The proposed methodology, on the other hand, relies on high quality adaptive integrators, which have no such stability problems.

Currently, efficient and robust MCMC computations has been a field dominated by tailor-making to specific applications and a large degree of craftsmanship. Effectively, the two above points reduces such MCMC computations into a more routine task of numerically integrating ordinary differential equations using adaptive/automatic methods.

There scope for substantial further work on CTHMC-processes beyond the initial developments given here. A, by no means complete, list of possible further research directions related to CTHMC processes is given in Appendix F.

References

- Alenlöv, J., A. Doucet, and F. Lindsten (2016). Pseudo-marginal Hamiltonian Monte Carlo. arXiv preprint arXiv:1607.02516.
- Baker, J., P. Fearnhead, E. B. Fox, and C. Nemeth (2019, May). Control variates for stochastic gradient MCMC. *Statistics and Computing* 29(3), 599–615.
- Betancourt, M. (2016). Identifying the optimal integration time in Hamiltonian Monte Carlo. arXiv:1601.00225.

- Bierkens, J., P. Fearnhead, and G. Roberts (2019, 06). The Zig-Zag process and super-efficient sampling for Bayesian analysis of big data. *Ann. Statist.* 47(3), 1288–1320.
- Bou-Rabee, N. and J. M. Sanz-Serna (2017, 08). Randomized Hamiltonian Monte Carlo. *Ann. Appl. Probab.* 27(4), 2159–2194.
- Bouchard-Côté, A., S. J. Vollmer, and A. Doucet (2018). The Bouncy Particle Sampler: A nonreversible rejection-free Markov chain Monte Carlo method. *Journal of the American Statistical Association* 113(522), 855–867.
- Cambanis, S., S. Huang, and G. Simons (1981). On the theory of elliptically contoured distributions. *Journal of Multivariate Analysis* 11(3), 368 – 385.
- Carpenter, B., A. Gelman, M. Hoffman, D. Lee, B. Goodrich, M. Betancourt, M. Brubaker, J. Guo, P. Li, and A. Riddell (2017). Stan: A probabilistic programming language. *Journal of Statistical Software* 76(1), 1–32.
- Chopin, N. and J. Ridgway (2017, 02). Leave Pima Indians alone: Binary regression as a benchmark for Bayesian computation. *Statist. Sci.* 32(1), 64–87.
- Cotter, S., T. House, and F. Pagani (2020). The NuZZ: Numerical ZigZag sampling for general models. arXiv:2003.03636.
- Davis, M. H. A. (1984). Piecewise-deterministic Markov processes: A general class of non-diffusion stochastic models. *Journal of the Royal Statistical Society: Series B (Methodological)* 46(3), 353–376.
- Davis, M. H. A. (1993). *Markov models and optimization*. Chapman & Hall, London.
- Dormand, J. and P. Prince (1987). Runge-Kutta-Nystrom triples. *Computers & Mathematics with Applications* 13(12), 937 – 949.
- Fang, Y., J. M. Sanz-Serna, and R. D. Skeel (2014). Compressible generalized hybrid Monte Carlo. *The Journal of Chemical Physics* 140(17), 174108.
- Fearnhead, P., J. Bierkens, M. Pollock, and G. O. Roberts (2018, 08). Piecewise deterministic Markov processes for continuous-time monte carlo. *Statist. Sci.* 33(3), 386–412.
- Franco, J. and I. Gómez (2014). Symplectic explicit methods of Runge-Kutta-Nyström type for solving perturbed oscillators. *Journal of Computational and Applied Mathematics* 260, 482–493.

- Gelman, A., J. B. Carlin, H. S. Stern, D. B. Dunson, A. Vehtari, and D. Rubin (2014). *Bayesian Data Analysis* (3 ed.). CRC Press.
- Geyer, C. J. (1992). Practical Markov chain Monte Carlo. *Statistical Science* 7(4), pp. 473–483.
- Girolami, M. and B. Calderhead (2011). Riemann manifold Langevin and Hamiltonian Monte Carlo methods. *Journal of the Royal Statistical Society: Series B (Statistical Methodology)* 73(2), 123–214.
- Goldstein, H., C. Poole, and J. Safko (2002). *Classical Mechanics* (3 ed.). Addison Wesley.
- Golosnoy, V., B. Gribisch, and R. Liesenfeld (2012). The conditional autoregressive wishart model for multivariate stock market volatility. *Journal of Econometrics* 167(1), 211 – 223.
- Grothe, O., T. S. Kleppe, and R. Liesenfeld (2019). The gibbs sampler with particle efficient importance sampling for state-space models. *Econometric Reviews* 38(10), 1152–1175.
- Hairer, E., S. P. Nørsett, and G. Wanner (1993). *Solving Ordinary Differential Equations I (2nd Revised Ed.): Nonstiff Problems*. Berlin, Heidelberg: Springer-Verlag.
- Hoffman, M. D. and A. Gelman (2014). The no-u-turn sampler: Adaptively setting path lengths in Hamiltonian Monte Carlo. *Journal of Machine Learning Research* 15, 1593–1623.
- Kleppe, T. S. (2018). Modified Cholesky Riemann manifold Hamiltonian Monte Carlo: exploiting sparsity for fast sampling of high-dimensional targets. *Statistics and Computing* 28(4), 795–817.
- Kleppe, T. S. (2019). Dynamically rescaled Hamiltonian Monte Carlo for Bayesian hierarchical models. *Journal of Computational and Graphical Statistics* 28(3), 493–507.
- Leimkuhler, B. and S. Reich (2004). *Simulating Hamiltonian dynamics*. Cambridge University Press.
- McCullagh, P. and J. A. Nelder (1989). *Generalized Linear Models, 2nd Ed.* New York: Chapman & Hall.
- Michie, D., D. J. Spiegelhalter, and C. C. Taylor (Eds.) (1994). *Machine Learning, Neural and Statistical Classification*. Series in Artificial Intelligence. Hemel Hempstead, Hertfordshire, England: Ellis Horwood.
- Neal, R. M. (2003). Slice sampling. *The Annals of Statistics* 31(3), 705–767.
- Neal, R. M. (2010). MCMC using Hamiltonian dynamics. In *Handbook of Markov Chain Monte Carlo*, pp. 113–162.
- Osmundsen, K. K., T. S. Kleppe, and R. Liesenfeld (2019). Importance sampling-based transport map Hamiltonian Monte Carlo for Bayesian hierarchical models. arXiv:1812.07929.

- Press, W. H., S. A. Teukolsky, W. T. Vetterling, and B. P. Flannery (2007). *Numerical Recipes 3rd Edition: The Art of Scientific Computing*. Cambridge University Press.
- Robert, C. P. and G. Casella (2004). *Monte Carlo Statistical Methods* (second ed.). Springer.
- Roberts, G. O. and J. S. Rosenthal (1998). Optimal scaling of discrete approximations to Langevin diffusions. *Journal of the Royal Statistical Society: Series B (Statistical Methodology)* 60(1), 255–268.
- Sanz-Serna, J. and M. Calvo (1994). *Numerical Hamiltonian Problems*. Dover Publications Inc, New York.
- Stan Development Team (2017). Stan modeling language users guide and reference manual, version 2.17.0.
- Vanetti, P., A. Bouchard-Côté, G. Deligiannidis, and A. Doucet (2017). Piecewise-deterministic Markov chain Monte Carlo. arXiv:1707.05296.
- Welling, M. and Y. W. Teh (2011). Bayesian learning via stochastic gradient Langevin dynamics. In *Proceedings of the 28th International Conference on International Conference on Machine Learning*, Madison, WI, USA, pp. 681–688. Omnipress.
- Wu, C. and C. P. Robert (2020). Coordinate sampler: a non-reversible Gibbs-like MCMC sampler. *Statistics and Computing* 30(3), 721–730.
- Wu, C., J. Stoehr, and C. P. Robert (2018). Faster Hamiltonian Monte Carlo by learning leapfrog scale. arXiv:1810.04449.

Online Appendix to “Connecting the Dots: Towards Continuous Time Hamiltonian Monte Carlo” by Tore Selland Kleppe

This version: July 19, 2022

In this online Appendix, equation numbers ≤ 27 refer to equations in the main article text.

A Details of derivations

A.1 The left-hand side of (5) is the Poisson bracket between p and \mathcal{H}

Suppose $D = 2d$, $\mathbf{z} = [\mathbf{q}^T, \mathbf{p}^T]^T$ and $\Phi(\mathbf{z})$ corresponds to Hamilton’s equations associated with separable Hamiltonian (1), i.e.

$$\Phi(\mathbf{z}) = \begin{bmatrix} \mathbf{M}^{-1}\mathbf{p} \\ \nabla_{\mathbf{q}} \log \tilde{\pi}(\mathbf{q}) \end{bmatrix} = \mathbf{J}\nabla_{\mathbf{z}}\mathcal{H}(\mathbf{z}), \quad \mathbf{J} = \begin{bmatrix} \mathbf{0}_{d,d} & \mathbf{I}_d \\ -\mathbf{I}_d & \mathbf{0}_{d,d} \end{bmatrix},$$

Then the left-hand side of the stationary Fokker-Planck equation (5) is equal to the Poisson Bracket $\{p, \mathcal{H}\}(\mathbf{z})$ (see e.g. Leimkuhler and Reich, 2004, Section 3.3) between the density $p(\mathbf{z})$ and the Hamiltonian $\mathcal{H}(\mathbf{z})$, namely

$$\begin{aligned} \{p, \mathcal{H}\}(\mathbf{z}) &:= [\nabla_{\mathbf{z}}p(\mathbf{z})]^T \mathbf{J}\nabla_{\mathbf{z}}\mathcal{H}(\mathbf{z}), \\ &= [\nabla_{\mathbf{q}}p(\mathbf{z})]^T \mathbf{M}^{-1}\mathbf{p} + [\nabla_{\mathbf{p}}p(\mathbf{z})]^T \nabla_{\mathbf{q}} \log \tilde{\pi}(\mathbf{q}), \\ &= \sum_{i=1}^d \frac{\partial}{\partial q_i} [\mathbf{M}^{-1}\mathbf{p}]_i p(\mathbf{z}) + \sum_{i=1}^d \frac{\partial}{\partial p_i} [\nabla_{\mathbf{q}} \log \tilde{\pi}(\mathbf{q})]_i p(\mathbf{z}), \\ &= \sum_{i=1}^D \frac{\partial}{\partial z_i} [\Phi_i(\mathbf{z})p(\mathbf{z})]. \end{aligned}$$

For any first integral, say $g(\mathbf{z})$ (i.e. conserved quantity so that $g(\varphi_t(\mathbf{z})) = g(\mathbf{z}) \forall t, \mathbf{z}$), the Poisson bracket between g and \mathcal{H} is zero for all \mathbf{z} . Clearly, the Boltzmann distribution $\rho(\mathbf{z}) \propto \exp(-\mathcal{H}(\mathbf{z}))$ is a first integral of \mathcal{H} , and hence $\{\mathcal{H}, \rho\}(\mathbf{z}) = \sum_{i=1}^D \frac{\partial}{\partial z_i} [\Phi_i(\mathbf{z})\rho(\mathbf{z})] = 0 \forall \mathbf{z}$.

A.2 Position-dependent event rates

For $Q(\mathbf{z}|\mathbf{z}') = \delta_{\mathbf{q}'}(\mathbf{q})\mathcal{N}(\mathbf{p}|\phi\mathbf{p}', \sqrt{1-\phi^2}\mathbf{M})$ and $\lambda(\mathbf{z}) = \omega(\mathbf{q})$, the integral on the right-hand side of (5) is given as

$$\begin{aligned}
& \int \int \pi(\mathbf{q}')\mathcal{N}(\mathbf{p}'|\mathbf{0}_d, \mathbf{M})\omega(\mathbf{q}')\delta(\mathbf{q} - \mathbf{q}')\mathcal{N}(\mathbf{p}|\phi\mathbf{p}', \sqrt{1-\phi^2}\mathbf{M})d\mathbf{q}'d\mathbf{p}', \\
& = \pi(\mathbf{q})\omega(\mathbf{q}) \int \mathcal{N}(\mathbf{p}'|\mathbf{0}_d, \mathbf{M})\mathcal{N}(\mathbf{p}|\phi\mathbf{p}', \sqrt{1-\phi^2}\mathbf{M})d\mathbf{p}', \\
& = \pi(\mathbf{q})\mathcal{N}(\mathbf{p}|\mathbf{0}_d, \mathbf{M})\omega(\mathbf{q}), \\
& = \rho(\mathbf{z})\lambda(\mathbf{z}),
\end{aligned}$$

and hence the right-hand side of (5) also vanishes for these choices of λ and Q and hence the resulting process is on target.

A.3 Details for momentum-dependent event rates

For the at event distribution (9), and an event rate depending on \mathbf{p} , the integral on the right-hand side of (5) is given as

$$\begin{aligned}
& \int \int \pi(\mathbf{q}')\mathcal{N}(\mathbf{p}'|\mathbf{0}_d, \mathbf{M})\lambda(\mathbf{q}', \mathbf{p}')\delta(\mathbf{q} - \mathbf{q}')\frac{\lambda(\mathbf{q}', \mathbf{p})\mathcal{N}(\mathbf{p}|\mathbf{0}, \mathbf{M})}{C(\mathbf{q}')}d\mathbf{q}'d\mathbf{p}' \\
& = \pi(\mathbf{q})\frac{\lambda(\mathbf{q}, \mathbf{p})\mathcal{N}(\mathbf{p}|\mathbf{0}, \mathbf{M})}{C(\mathbf{q})} \underbrace{\int \mathcal{N}(\mathbf{p}'|\mathbf{0}_d, \mathbf{M})\lambda(\mathbf{q}, \mathbf{p}')d\mathbf{p}'}_{=C(\mathbf{q})} \\
& = \pi(\mathbf{q})\mathcal{N}(\mathbf{p}|\mathbf{0}, \mathbf{M})\lambda(\mathbf{q}, \mathbf{p}) \\
& = \rho(\mathbf{z})\lambda(\mathbf{z}),
\end{aligned}$$

and hence the right-hand side of (5) also vanishes for these choices of λ and Q and hence the resulting process is on target.

A.4 Riemann manifold variants

This section gives the relevant details for constructing continuous time Riemann manifold HMC processes. Such processes rely on selecting a symmetric positive definite “metric tensor” $\mathbf{G}(\mathbf{q}) \in \mathbb{R}^{d \times d}$ which should reflect the “local” precision of the target distribution around \mathbf{q} . The non-separable Hamiltonian \mathcal{K} typically

used in such situations is given by (Girolami and Calderhead, 2011)

$$\mathcal{K}(\mathbf{z}) = -\log \tilde{\pi}(\mathbf{q}) + \frac{1}{2} \log(|\mathbf{G}(\mathbf{q})|) + \frac{1}{2} \mathbf{p}^T \mathbf{G}(\mathbf{q})^{-1} \mathbf{p}.$$

Hamilton's equations are still given by

$$\Phi(\mathbf{z}) = \mathbf{J} \nabla_{\mathbf{z}} \mathcal{K}(\mathbf{z}) = \begin{bmatrix} \nabla_{\mathbf{p}} \mathcal{K}(\mathbf{z}) \\ -\nabla_{\mathbf{q}} \mathcal{K}(\mathbf{z}) \end{bmatrix},$$

and Boltzmann distribution by $\rho(\mathbf{z}) = \pi(\mathbf{q}) \mathcal{N}(\mathbf{p}|\mathbf{0}, \mathbf{G}(\mathbf{q})) = \exp(-\mathcal{K}(\mathbf{z})) W^{-1}$, $W = \int \exp(-\mathcal{K}(\mathbf{z})) d\mathbf{z}$. In terms of numerical implementation, it is seen that Hamilton's equations cannot in this case be reduced to a second order ODE but may still be solved using general purpose first order ODE solvers such as Runge-Kutta methods. A drawback of general Riemann manifold HMC methods is that symplectic integrators for non-separable Hamiltonians are necessary implicit, and hence require many evaluations of Φ per integration step. A pro of the proposed methodology is that adaptive explicit solvers may be used.

The strategy for showing that the drift term in the Fokker-Planck equation (5) vanishes also with Hamiltonian \mathcal{K} is to look directly at the drift term with $p = \rho$. In this case

$$\begin{aligned} \sum_{i=1}^D \frac{\partial}{\partial z_i} [\Phi_i \rho(\mathbf{z})] &= W^{-1} \sum_{i=1}^d \frac{\partial}{\partial q_i} \left[\exp(-\mathcal{K}(\mathbf{z})) \frac{\partial}{\partial p_i} \mathcal{K}(\mathbf{z}) \right] \\ &\quad - W^{-1} \sum_{i=1}^d \frac{\partial}{\partial p_i} \left[\exp(-\mathcal{K}(\mathbf{z})) \frac{\partial}{\partial q_i} \mathcal{K}(\mathbf{z}) \right], \\ &= -\rho(\mathbf{z}) \sum_{i=1}^d \left[\frac{\partial}{\partial q_i} \mathcal{K}(\mathbf{z}) \right] \left[\frac{\partial}{\partial p_i} \mathcal{K}(\mathbf{z}) \right] \\ &\quad + \rho(\mathbf{z}) \sum_{i=1}^d \frac{\partial^2}{\partial q_i \partial p_i} \mathcal{K}(\mathbf{z}) \\ &\quad + \rho(\mathbf{z}) \sum_{i=1}^d \left[\frac{\partial}{\partial p_i} \mathcal{K}(\mathbf{z}) \right] \left[\frac{\partial}{\partial q_i} \mathcal{K}(\mathbf{z}) \right] \\ &\quad - \rho(\mathbf{z}) \sum_{i=1}^d \frac{\partial^2}{\partial p_i \partial q_i} \mathcal{K}(\mathbf{z}), \\ &= 0. \end{aligned}$$

(For clarity; the second equality is based on the chain rule $\frac{\partial}{\partial z_i} \exp(-\mathcal{K}(\mathbf{z})) \Phi_i(\mathbf{z}) = -\exp(-\mathcal{K}(\mathbf{z})) \Phi_i(\mathbf{z}) \frac{\partial}{\partial z_i} \mathcal{K}(\mathbf{z}) + \exp(-\mathcal{K}(\mathbf{z})) \frac{\partial}{\partial z_i} \Phi_i(\mathbf{z})$).

As also the flow associated with \mathcal{K} preserves the Boltzmann distribution, one is also in this case free

to choose the event specification solely on making the right-hand side of (5) vanish. Essentially the same event specification cases as in the separable case, with minimal modifications to account for the position-dependence in the Boltzmann distribution \mathbf{p} -marginal, applies. I.e.

$$\lambda(\mathbf{z}) = \omega(\mathbf{q}), \quad Q(\mathbf{p}|\mathbf{z}') = \mathcal{N}(\mathbf{p}|\phi\mathbf{p}', \sqrt{1-\phi^2}\mathbf{G}(\mathbf{q}')),$$

and

$$\lambda(\mathbf{z}) = \lambda(\mathbf{q}, \mathbf{p}), \quad Q(\mathbf{p}|\mathbf{z}') \propto \lambda(\mathbf{q}', \mathbf{p})\mathcal{N}(\mathbf{p}|\mathbf{0}_d, \mathbf{G}(\mathbf{q}')),$$

lead to on target processes. The arguments leading to this conclusion are analogous to those in Appendixes A.2, A.3 and are not repeated.

A.5 Langevin limit

To obtain the Langevin limit under event specification 1, consider first a large, but finite λ , and condition on a sequence of inter-event times $\tau_i \sim \text{iid } \text{Exp}(\lambda^{-1})$ $i = 1, 2, \dots$. A time-discretized version of the PDP \mathcal{Z}_t , say $\tilde{\mathbf{z}}_j = [\tilde{\mathbf{q}}_j^T, \tilde{\mathbf{p}}_j^T]^T \approx \mathcal{Z}_{\sum_{i=1}^j \tau_i}$, obtains by first applying a single leap-frog step (with time step τ_i) to each deterministic transition to get the state immediately before the $(i+1)$ th event, say $\tilde{\mathbf{z}}_{i+1}^*$:

$$\tilde{\mathbf{p}}_{i+1/2} = \tilde{\mathbf{p}}_i + \frac{\tau_{i+1}}{2} \nabla_{\mathbf{q}} \log \tilde{\pi}(\tilde{\mathbf{q}}_i), \quad (28)$$

$$\tilde{\mathbf{q}}_{i+1}^* = \tilde{\mathbf{q}}_i + \tau_{i+1} \mathbf{M}^{-1} \tilde{\mathbf{p}}_{i+1/2}, \quad (29)$$

$$\tilde{\mathbf{p}}_{i+1}^* = \tilde{\mathbf{p}}_{i+1/2} + \frac{\tau_{i+1}}{2} \nabla_{\mathbf{q}} \log \tilde{\pi}(\tilde{\mathbf{q}}_{i+1}^*).$$

(the latter equation is not needed but is given for completeness of the leapfrog step). Secondly, at the event (at time $\sum_{j=1}^{i+1} \tau_j$) $\tilde{\mathbf{z}}_{i+1}$ is sampled according to $Q(\cdot|\tilde{\mathbf{z}}_{i+1}^*)$, which reduces to:

$$\tilde{\mathbf{q}}_{i+1} = \tilde{\mathbf{q}}_{i+1}^* \quad (30)$$

$$\tilde{\mathbf{p}}_{i+1} = \varepsilon_{i+1}, \quad \varepsilon_{i+1} \sim \text{iid } N(\mathbf{0}_{d,1}, \mathbf{M}). \quad (31)$$

Now, since the time-discrete momentum is resampled each step, the discrete time (marginal) position dynamics $\tilde{\mathbf{q}}_i$ obtains by combining (28,30) and time-shifted (31) into (29):

$$\tilde{\mathbf{q}}_{i+1} = \tilde{\mathbf{q}}_i + \frac{\tau_{i+1}^2}{2} \mathbf{M}^{-1} \nabla_{\mathbf{q}} \log \tilde{\pi}(\tilde{\mathbf{q}}_i) + \tau_i \mathbf{M}^{-\frac{1}{2}} \eta_i, \quad (32)$$

where $\eta_i = \mathbf{M}^{-\frac{1}{2}} \varepsilon_i \sim N(\mathbf{0}_{d,1}, \mathbf{I}_d)$. Equation 32 is recognized to be the Euler-Maruyama discretization of (10) with time step size τ_{i+1}^2 . Finally, upon letting $\lambda \rightarrow \infty$, the discrete time process $\tilde{\mathbf{z}}_j$ converges to the underlying PDP, and $\tilde{\mathbf{q}}_j$ to the Langevin process (10) a.s.

A.6 Arc-length and event specification 3

Consider the calculation of the arc-length of some (position) dynamics $\mathbf{q}(s)$, $s \in [0, t]$ using the distance

$$d(\mathbf{q}, \mathbf{q}') = \sqrt{(\mathbf{q} - \mathbf{q}')^T \mathbf{M} (\mathbf{q} - \mathbf{q}')}$$

Notice that throughout this text, \mathbf{M}^{-1} should reflect $\text{Var}(\mathbf{q})$ and hence the distance d aims at making the contribution of each dimension more uniform. Discretizing time $s_i = i\Delta$, $\Delta = t/N$, the arc-length may be arbitrarily well approximated by

$$\begin{aligned} A_N &= \sum_{i=1}^N \sqrt{(\mathbf{q}(s_i) - \mathbf{q}(s_{i-1}))^T \mathbf{M} (\mathbf{q}(s_i) - \mathbf{q}(s_{i-1}))}, \\ &= \sum_{i=1}^N \Delta \sqrt{\left[\frac{\mathbf{q}(s_i) - \mathbf{q}(s_{i-1})}{\Delta} \right]^T \mathbf{M} \left[\frac{\mathbf{q}(s_i) - \mathbf{q}(s_{i-1})}{\Delta} \right]}, \end{aligned}$$

for large N . Letting $N \rightarrow \infty$ one obtains by a standard limit argument that

$$A_N \rightarrow A = \int_0^t \sqrt{[\dot{\mathbf{q}}(s)]^T \mathbf{M} \dot{\mathbf{q}}(s)} ds.$$

Finally, from the first of Hamilton's equations, $\dot{\mathbf{q}}(s) = \mathbf{M}^{-1} \mathbf{p}(s)$:

$$A = \int \sqrt{\mathbf{p}(s)^T \mathbf{M}^{-1} \mathbf{p}(s)} ds$$

which is (up to a multiplicative constant) the integrated $\lambda(\mathbf{z})$ (4) used in event specification 3.

B Temporal averages of the Hamiltonian dynamics for Gaussian targets

This section considers the temporal average of the flow for *Gaussian* targets. In particular it is shown that exploring only a single energy levelset is sufficient to get asymptotically correct estimates for any linear combination of the mean of the target when continuous sampling is employed.

Consider a $N(\mu, \Sigma)$ target distribution, where Σ is positive definite and finite. The Hamiltonian dynamics

$\mathbf{z}(t)$ is then the solution to the linear differential equation

$$\dot{\mathbf{z}}(t) = \mathbf{B}\mathbf{z}(t) + \mathbf{b} \quad (33)$$

where

$$\mathbf{B} = \begin{bmatrix} \mathbf{0}_{d,d} & \mathbf{M}^{-1} \\ -\Sigma^{-1} & \mathbf{0}_{d,d} \end{bmatrix}, \quad \mathbf{b} = \begin{bmatrix} \mathbf{0}_{d,1} \\ \Sigma^{-1}\mu \end{bmatrix}.$$

Consider first the case where $\mu = \mathbf{0}_d$, which results in the solution to (33) given by $\mathbf{z}(t) = \exp(t\mathbf{B})\mathbf{z}(0)$ where $\exp(t\mathbf{B})$ is the matrix exponential of matrix $t\mathbf{B}$. This solution necessarily conserves the associated Hamiltonian, which may be written as

$$\mathcal{H}(\mathbf{z}(t)) = \frac{1}{2}\mathbf{z}(t)^T \mathbf{B}^* \mathbf{z}(t), \quad \mathbf{B}^* = \begin{bmatrix} \Sigma^{-1} & \mathbf{0}_{d,d} \\ \mathbf{0}_{d,d} & \mathbf{M}^{-1} \end{bmatrix}. \quad (34)$$

From the conservation of (34), it is clear that the solutions $\mathbf{z}(t)$ are restricted to an ellipsoid (centered in $\mathbf{0}_{2d,1}$) in \mathbb{R}^{2d} , and hence $\exp(t\mathbf{B})\mathbf{v} = O(1)$ as $t \rightarrow \infty$ for any finite vector $\mathbf{v} \in \mathbb{R}^{2d}$.

Now, consider the general $\mu \in \mathbb{R}^d$ case. Any linear algebra textbook provides the solution to (33), in terms of an initial state $\mathbf{z}(0)$, namely

$$\mathbf{z}(t) = \exp(t\mathbf{B})\mathbf{z}(0) + \mathbf{B}^{-1}[\exp(t\mathbf{B}) - \mathbf{I}_{2d}]\mathbf{b}.$$

Suppose now that we seek the temporal average of some linear combination, say $\mathbf{K}\mathbf{z}(t)$, $\mathbf{K} \in \mathbb{R}^{l \times 2d}$, of the dynamics:

$$\begin{aligned} \frac{1}{T} \int_0^T \mathbf{K}\mathbf{z}(t)dt &= \frac{1}{T}\mathbf{K} \left[\int_0^T \exp(t\mathbf{B})dt \right] \mathbf{z}(0) + \frac{1}{T}\mathbf{K}\mathbf{B}^{-1} \left[\int_0^T \exp(t\mathbf{B})dt \right] \mathbf{b} - \mathbf{K}\mathbf{B}^{-1}\mathbf{b} \\ &= \frac{1}{T}\mathbf{K}\mathbf{B}^{-1}[\exp(T\mathbf{B}) - \mathbf{I}_{2d}]\mathbf{z}(0) \\ &\quad + \frac{1}{T}\mathbf{K}\mathbf{B}^{-1}\mathbf{B}^{-1}[\exp(T\mathbf{B}) - \mathbf{I}_{2d}]\mathbf{b} \\ &\quad + \mathbf{K}[\mu^T, \mathbf{0}_{d,1}^T]^T. \end{aligned}$$

Now, former two terms in the latter representation of $\frac{1}{T} \int_0^T \mathbf{K}\mathbf{z}(t)dt$ vanishes as $T \rightarrow \infty$, (since $\mathbf{K}\mathbf{B}^{-1}[\exp(T\mathbf{B}) -$

$\mathbf{I}_{2d}\mathbf{z}(0) = O(1)$ and $\mathbf{KB}^{-1}\mathbf{B}^{-1}[\exp(T\mathbf{B}) - \mathbf{I}_{2d}]\mathbf{b} = O(1)$, and one may conclude that

$$\frac{1}{T} \int_0^T \mathbf{K}\mathbf{z}(t)dt \xrightarrow{T \rightarrow \infty} \mathbf{K} \begin{bmatrix} \mu \\ \mathbf{0}_{d,1} \end{bmatrix},$$

invariantly of $\mathbf{z}(0)$ (or equivalently the energy level set $\mathbf{z}(t)$ is restricted to).

For the interested reader; a further special case obtains when the mass matrix is chosen to be the precision of the target, i.e. $\mathbf{M} = \Sigma^{-1}$. Then the centered flow takes a particularly simple form:

$$\exp(t\mathbf{B}) = \begin{bmatrix} \cos(t)\mathbf{I}_{d,d} & \sin(t)\Sigma \\ -\sin(t)\Sigma & \cos(t)\mathbf{I}_{d,d} \end{bmatrix}.$$

(This latter expression obtains from that even powers of \mathbf{B} are $\pm\mathbf{I}_{2d}$ and odd powers of \mathbf{B} are $\pm\mathbf{B}$, and subsequently employing this information in infinite series defining $\exp(t\mathbf{B})$.) In this case, the former two terms in the latter representation of $\frac{1}{T} \int_0^T \mathbf{K}\mathbf{z}(t)dt$ above vanishes whenever $t = 2\pi k$, k is an integer. I.e. the trajectory forms exactly k closed orbits centered in μ on the underlying ellipsoid, and the average then becomes μ . For $\mathbf{M} \neq \Sigma^{-1}$, the time T_i required for $T_i^{-1} \int_0^{T_i} q_i(t)dt = \mu_i$ generally depends on i , and thus only the asymptotic result above holds in this case.

C Details related to numerical implementation

Denote by ψ_ε the RKN step. Then $\hat{\mathbf{s}}(\tau + \varepsilon) = \psi_\varepsilon(\mathbf{s}(\tau))$, starting at $\mathbf{s}(\tau)$ and with time step size ε , is a 6th order approximation of the flow. In addition, when ψ_ε has been evaluated, the following is available at negligible additional cost (in particular no further evaluations of the right-hand side of (15)):

1. A 4th order approximation, say $\tilde{\mathbf{s}}(\tau + \varepsilon)$, of $\mathbf{s}(\tau + \varepsilon)$ used for estimation of the (local) error incurred, which is subsequently used in the adaptive step size selection.
2. A 6th order interpolation approximation, say $\hat{\mathbf{s}}(\tau + \xi\varepsilon)$, of any element of $(\mathbf{q}(\tau + \xi\varepsilon), \dot{\mathbf{q}}(\tau + \xi\varepsilon), \mathbf{r}(\tau + \xi\varepsilon))$, $\xi \in (0, 1)$.

A fairly standard PI-step size controller (see e.g. Press et al., 2007, Section 17.2.1) was used to select ε dynamically, by maintaining that

$$\max_i \frac{|\hat{\mathbf{s}}_i(\tau + \varepsilon) - \tilde{\mathbf{s}}_i(\tau + \varepsilon)|}{tol_a + tol_r |\hat{\mathbf{s}}_i(\tau + \varepsilon)|} < 1$$

for all time RKN steps. Here, tol_a and tol_r are the absolute- and relative error tolerances respectively, which must be chosen a-priori.

Algorithm 1 Basic CTHMC algorithm based on modified RKN integrator. Notice, this formulation assumes that the event intensity λ depends on \mathbf{q} only. The algorithm produces both continuous time estimates (6) of the given moments, and discrete time samples \mathbf{S} which may be used similarly to conventional MCMC samples.

Input: Target log-density kernel $\log \tilde{\pi}(\mathbf{q})$, $\mathbf{q} \in \mathbb{R}^d$ associated with target density $\pi(\mathbf{q})$.
Input: Event specification (λ, Q) (see e.g. Table 1).
Input: Mass matrix $\mathbf{M} \in \mathbb{R}^{d \times d}$, symmetric, positive definite (e.g. $\mathbf{M} = \mathbf{I}_d$).
Input: Simulation time span $T \in \mathbb{R}^+$.
Input: Number of discrete time samples N .
Input: Initial position $\mathbf{q}_0 \in \mathbb{R}^d$.
Input: Numerical error tolerances tol_a, tol_r (e.g. $tol_a = tol_r = 1.0e - 3$).
Input: Moments $g_1, \dots, g_m, g_k : \mathbb{R}^d \mapsto \mathbb{R}$, $k = 1, \dots, m$, for which $\int g_k(\mathbf{q})\pi(\mathbf{q})d\mathbf{q}$ are to be estimated.

Define integrated quantities $\mathcal{M}(\mathbf{q}) = [\lambda(\mathbf{q}), g_1(\mathbf{q}), \dots, g_m(\mathbf{q})] : \mathbb{R}^d \mapsto \mathbb{R}^{m+1}$.

```

t ← 0,                                     ▷ Continuous time process time.
Q(0) ← q0.                                 ▷ Initial q configuration.
P(0) ~ N(0d, M).                            ▷ Initial p configuration (in case of autocorrelated momentum refreshes)
g ← 0m                                       ▷ Storage for estimated moments.
S ← 0d,M                                     ▷ Storage for discrete time samples.
i ← 1                                       ▷ Discrete samples counter.
while t < T do                               ▷ Main loop over events
  P(t) ~ Q(·|Z(t-)).                         ▷ Simulate new momentum
  u ~ Exp(1).                                 ▷ See equation 4
  ŝ(0) ← (Q(t), M-1P(t), 0m+1).           ▷ Initial conditions for system of ODEs (15)
  τ ← 0.                                       ▷ Hamiltonian dynamics (between-events) time.
  while ŝ2d+1(τ) < u and t + τ < T do
    Propose a new step size ε.                 ▷ Recall ŝ2d+1(τ) ≈ ∫0τ λ(q(v))dv
    ε ← min(ε, T - (t + τ))                 ▷ Using e.g. PI step size controller.
    ŝ(τ + ε) = ψε(ŝ(τ)) for ODE (15)        ▷ No simulation beyond process time t = T.
    ξ ← 1                                     ▷ The RKN step
    if ŝ2d+1(τ + ε) > u then                 ▷ "If(event occurred during this integration step)"
      Find ξ so that ŝ2d+1(τ + ξε) = u      ▷ Time between-events was τ + ξε.
    end if
    Q(t + τ + r) ← ŝ1:d(τ + r), r ∈ [0, ξε] ▷ Position q.
    P(t + τ + r) ← Mŝd+1:2d(τ + r), r ∈ [0, ξε] ▷ Momentum p.
    while τ + ξε ≥ iT/N do                 ▷ The ith sample during current integration step?
      S1:d,i ← Q(iT/N)                    ▷ Collect sample (in practice done using RKN step interpolation).
      i ← i + 1                             ▷ Advance discrete time samples counter.
    end while
    τ ← τ + ε                               ▷ Update Hamiltonian dynamics time
  end while                                 ▷ Hamiltonian dynamics integration loop
  t ← t + (τ - ε) + ξε.                    ▷ Update process time t
  g ← g + ŝ2d+2:2d+1+m((τ - ε) + ξε)      ▷ t-1g estimates moments
end while                                  ▷ Event loop

Return T-1g                               ▷ T-1gk → ∫ gk(q)π(q)dq as T → ∞.
Return S.   ▷ The columns of S are dependent random draws whose marginal distribution approaches π(q).

```

A quite general outline of the numerical algorithm for simulating CTHMC processes is given in Algorithm 1. The outlined algorithm produces both integrated moments approximating $\int g_k(\mathbf{q})\pi(\mathbf{q})d\mathbf{q}$, $k = 1, \dots, m$ based on (6) and discrete time samples \mathbf{S} . Notice that Algorithm 1 assumes event intensities not depending on the momentum coordinate. However, it is straight forward to extend to the Algorithm to account for momentum-dependent event-rates based on the interpolation option of the RKN step.

D The salamander mating data using crossed random effects

For the purpose of further benchmarking of the proposed methodology against rstan, this section considers a crossed random effects model for the Salamander mating data of McCullagh and Nelder (1989, chap 14.5). The formulation of the model is an example model for INLA (see Salamander Model B at <http://www.r-inla.org/examples/volume-ii>), the particular parameterization is taken from Kleppe (2019, Section 5.3, "Full CIP/DRHMC") and the rstan implementation is identical to that of Kleppe (2019). The model is characterized by random effects precision priors

$$\begin{aligned} \tau_F &\sim \text{Gamma}(1, 0.622), \quad \tau_M \sim \text{Gamma}(1, 0.622), \\ \mathbf{P}_F &\sim \text{Wishart}_2(3.0, \mathbf{W}), \quad \mathbf{P}_M \sim \text{Wishart}_2(3.0, \mathbf{W}), \quad \mathbf{W} = \text{diag}(0.804, 0.804), \end{aligned}$$

random effects

$$[\mathbf{b}_{i1}^F, \mathbf{b}_{i2}^F]^T \sim \text{iid } N(\mathbf{0}_2, \mathbf{P}_F^{-1}), \quad i = 1, \dots, 20, \quad (35)$$

$$[\mathbf{b}_{j1}^M, \mathbf{b}_{j2}^M]^T \sim \text{iid } N(\mathbf{0}_2, \mathbf{P}_M^{-1}), \quad j = 1, \dots, 20, \quad (36)$$

$$\mathbf{b}_{i3}^F \sim \text{iid } N(0, \tau_F^{-1}), \quad i = 1, \dots, 20,$$

$$\mathbf{b}_{j3}^M \sim \text{iid } N(0, \tau_M^{-1}), \quad j = 1, \dots, 20,$$

and finally the observation equation

$$\mathbf{y}_{ijk} | \mathbf{\Pi}_{ijk} \sim \text{Bernoulli}(\mathbf{\Pi}_{ijk}), \quad \text{logit}(\mathbf{\Pi}_{ijk}) = \mathbf{x}_{ijk}^T \beta + \mathbf{b}_{ik}^F + \mathbf{b}_{jk}^F.$$

The observations are coded as 1 for successful mating of female salamander i and male salamander j in experiment $k = 1, 2, 3$. The salamanders in experiment $k = 1, 2$ are identical, and therefore their associated random effects (35,36) are allowed to be correlated. Finally, $\mathbf{x}_{ijk} \in \mathbb{R}^5$ is a covariate vector and $\beta \in \mathbb{R}^5$ is a fixed effect with flat prior. Experiment outcomes were recorded in 360 combinations of i, j, k .

	sampling	Prec(\mathbf{b}_{i1}^F)	Prec(\mathbf{b}_{i2}^F)	corr($\mathbf{b}_{i1}^F, \mathbf{b}_{i2}^F$)	Prec(\mathbf{b}_{i1}^M)	Prec(\mathbf{b}_{i2}^M)	corr($\mathbf{b}_{i1}^M, \mathbf{b}_{i2}^M$)	τ_F	τ_M	\mathbf{b}_{\cdot}	β
rstan, total sampling CPU time: 23.43 s											
post. mean		1.09	0.95	-0.08	1.55	1.11	0.63	2.19	0.74		
post. sd		0.94	0.79	0.40	1.20	0.89	0.26	1.51	0.59		
ESS/CPU time		241	217	103	194	226	137	356	235	≥ 243	≥ 178
pdphmc, event specification 1, $\gamma = 3$, total CPU time: 15.19 s											
post. mean	D	1.07	0.92	-0.09	1.52	1.09	0.64	2.13	0.68		
post. sd	D	0.91	0.77	0.40	1.18	0.84	0.26	1.52	0.49		
ESS/CPU time	D	149	188	155	274	244	200	333	252	≥ 319	≥ 191
ESS/CPU time	C	137	145	155	246	156	201	352	159	≥ 339	≥ 198
pdphmc, event specification 1, $\gamma = 10.0$, mean CPU time: 14.91 s											
post. mean	D	1.08	0.91	-0.08	1.55	1.12	0.62	2.25	0.74		
post. sd	D	0.91	0.75	0.40	1.21	0.91	0.26	1.56	0.55		
ESS/CPU time	D	244	316	164	339	313	206	344	320	≥ 326	≥ 215
ESS/CPU time	C	142	326	164	355	321	207	365	329	≥ 347	$\geq \mathbf{224}$
pdphmc, event specification 3, $\gamma = 3.0$, total CPU time: 14.69 s											
post. mean	D	1.09	0.91	-0.08	1.55	1.13	0.63	2.14	0.73		
post. sd	D	0.91	0.74	0.40	1.17	0.89	0.26	1.50	0.56		
ESS/CPU time	D	265	279	160	246	316	209	339	189	≥ 330	≥ 204
ESS/CPU time	C	208	186	161	221	250	210	357	128	$\geq \mathbf{352}$	≥ 209
pdphmc, event specification 3, $\gamma = 10.0$, total CPU time: 15.25 s											
post. mean	D	1.09	0.93	-0.08	1.53	1.13	0.62	2.22	0.71		
post. sd	D	0.90	0.77	0.40	1.15	0.88	0.27	1.59	0.54		
ESS/CPU time	D	270	318	159	322	297	198	338	310	≥ 321	≥ 208
ESS/CPU time	C	198	327	159	271	254	200	359	132	≥ 342	≥ 216

Table 6: Results for the Salamander mating experiment. The table gives posterior means (post. mean), posterior standard deviations (post. sd.), and also the number of effective samples produced per second of computing time (ESS/CPU time). For rstan, the results are based on 10 independent chains with 1000 transitions proceeding 1000 warmup transitions. For pdphmc, the results are based on trajectories of length $T = 2,000$ with the first half discarded as warmup and VARI mass. The post warmup period was discretely (D) sampled $N = 1000$ times and also continuous (C) samples were recorded. The former 8 columns focus on the posterior random effects precision structure, where (unconditional) precisions are denoted by “Prec” and correlations by “corr”. The last two columns give the worst case time-weighted ESSes for the random- and fixed effects respectively. The best overall sampling efficiencies are indicated with **bold** font.

	rstan		pdphmc		pdphmc	
			event spec. 1		event spec. 3	
	post. mean	post. SD	post. mean	post. SD	post. mean	post. SD
μ_1	4.15	0.199	4.16	0.206	4.16	0.202
μ_2	4.12	0.263	4.12	0.244	4.12	0.268
μ_3	3.71	0.154	3.72	0.149	3.72	0.154
μ_4	4.11	0.095	4.11	0.092	4.11	0.092
μ_5	3.53	0.136	3.53	0.134	3.53	0.132
σ_1	0.31	0.009	0.31	0.009	0.31	0.009
σ_2	0.26	0.008	0.26	0.008	0.26	0.008
σ_3	0.29	0.009	0.29	0.009	0.29	0.009
σ_4	0.28	0.009	0.28	0.009	0.28	0.009
σ_5	0.25	0.009	0.25	0.009	0.25	0.009
δ_1	0.97	0.005	0.97	0.005	0.97	0.005
δ_2	0.98	0.004	0.98	0.004	0.98	0.004
δ_3	0.96	0.006	0.96	0.006	0.96	0.006
δ_4	0.94	0.008	0.94	0.008	0.94	0.008
δ_5	0.96	0.006	0.96	0.006	0.96	0.006
$\mathbf{H}_{2,1}$	0.39	0.003	0.39	0.003	0.39	0.003
$\mathbf{H}_{3,1}$	0.29	0.003	0.29	0.003	0.29	0.003
$\mathbf{H}_{4,1}$	0.29	0.003	0.29	0.003	0.29	0.003
$\mathbf{H}_{5,1}$	0.23	0.002	0.23	0.002	0.23	0.002
$\mathbf{H}_{3,2}$	0.20	0.003	0.20	0.003	0.20	0.003
$\mathbf{H}_{4,2}$	0.17	0.003	0.17	0.003	0.17	0.003
$\mathbf{H}_{5,2}$	0.12	0.002	0.12	0.002	0.12	0.002
$\mathbf{H}_{4,3}$	0.22	0.004	0.22	0.004	0.22	0.004
$\mathbf{H}_{5,3}$	0.18	0.003	0.18	0.003	0.18	0.003
$\mathbf{H}_{5,4}$	0.11	0.002	0.11	0.002	0.11	0.002
ν	33.61	0.291	33.61	0.289	33.61	0.278

Table 7: Posterior means and standard deviations for the parameters of the dynamic inverted Wishart model of Section 6. Only results based on discrete samples are presented for the pdphmc methods, as the continuous samples means are identical to the discrete samples means in the precision reported here.

Details on the parameterization of model, aiming at making the target distribution suitable for HMC sampling by reducing “funnel” effects, are given in Kleppe (2019). Still the target distribution is quite far from being Gaussian. In total, the model involves $d = 133$ free parameters and random effects to be sampled.

Table 6 provides results, focusing on the posterior marginal precisions and correlations of random effects, as these are typically rather difficult to estimate using MCMC. The overall picture from the experiment is that pdphmc is slightly more efficient than rstan.

E Dynamic inverted Wishart model details

The priors and transformations to a unrestricted domain for the parameters are given by

- $\delta_g \sim \text{iid } \text{Uniform}(-1, 1)$, $g = 1, \dots, G$. Sampling was performed in a scaled logit-transformed param-

eter.

- $\boldsymbol{\mu}_g \sim \text{iid } N(0, 5^2)$, $g = 1, \dots, G$. No transformation applied.
- $\sigma_g^2 \sim \text{iid } p_0 s_0 / \chi_{p_0}^2$, $g = 1, \dots, G$, where $p_0 = 4$ and $s_0 = 0.25$. Sampling was performed in $\log(\sigma_g)$.
- $\mathbf{H}_{i,j} \sim \text{iid } N(0, 10^2)$, $j = 1, \dots, G-1, i = j+1, \dots, G$. No transformation applied.
- $\nu \sim \text{Uniform}(10.0, 60.0)$, Sampling was performed in a scaled logit-transformed parameter.

A fortunate property of this model, owing to the particular choice of observation equation (24) and scale matrix (25) is that $p(\mathbf{x}|\mathbf{Y}_{1:n}, \boldsymbol{\theta})$ factorizes as $\prod_{g=1}^G p(\mathbf{x}_{g,1:n}|\boldsymbol{\theta})h(\mathbf{x}_{g,1:n})$, i.e. the latent factors are conditionally on $\mathbf{Y}_{1:n}, \boldsymbol{\theta}$ independent over g . Moreover the function $h(\mathbf{x}_{g,1:n})$ has a particularly simple form

$$h(\mathbf{x}_{g,1:n}) \propto \prod_{k=1}^n \exp \left[\frac{\nu}{2} \mathbf{x}_{g,k} - \frac{\tilde{\mathbf{y}}_{g,k}}{2} \exp(\mathbf{x}_{g,k}) \right], \quad \tilde{\mathbf{y}}_{g,k} = [\mathbf{H}_{1:G,g}]^T \mathbf{Y}_k^{-1} [\mathbf{H}_{1:G,g}].$$

I.e. $p(\mathbf{x}|\mathbf{Y}_{1:n}, \boldsymbol{\theta})$ factorizes into the form of G independent (conditional on $\boldsymbol{\theta}$) smoothing distributions associated with single-dimensional state space models.

The transport map (see Osmundsen et al., 2019, for more details) $\gamma_{\boldsymbol{\theta}}$ relating \mathbf{x} and \mathbf{z} is given by

$$\mathbf{x}_{g,1:n} = \mathbf{h}_{g,\boldsymbol{\theta}} + \mathbf{L}_{g,\boldsymbol{\theta}}^{-T} \mathbf{z}_{(g-1)n+1:gn}, \quad g = 1, \dots, G$$

where $\mathbf{L}_{g,\boldsymbol{\theta}}$ is the lower Cholesky triangle of the SPD tri-diagonal matrix

$$\mathbf{G}_{g,\boldsymbol{\theta}} = \mathbf{G}_{g,\mathbf{x}|\boldsymbol{\theta}} + \mathbf{G}_{g,\mathbf{y}|\mathbf{x},\boldsymbol{\theta}}.$$

Here $\mathbf{G}_{g,\mathbf{x}|\boldsymbol{\theta}}$ is the (tri-diagonal) precision matrix of $\mathbf{x}_{g,1:n}|\boldsymbol{\theta}$ and $\mathbf{G}_{g,\mathbf{y}|\mathbf{x},\boldsymbol{\theta}}$ is the (diagonal) negative Hessian of $\mathbf{x}_{g,1:n} \mapsto \log(h(\mathbf{x}_{g,1:n}))$ evaluated at $\mathbf{h}_{g,\mathbf{y}|\mathbf{x},\boldsymbol{\theta}} = \arg \max_{\mathbf{x}_{g,1:n}} \log(h(\mathbf{x}_{g,1:n}))$ (this optimization problem splits into n separate single variable problems and is analytically solved). Finally

$$\mathbf{h}_{g,\boldsymbol{\theta}} = \mathbf{G}_{g,\boldsymbol{\theta}}^{-1} [\mathbf{G}_{g,\mathbf{x}|\boldsymbol{\theta}} E(\mathbf{x}_{g,1:n}|\boldsymbol{\theta}) + \mathbf{G}_{g,\mathbf{y}|\mathbf{x},\boldsymbol{\theta}} \mathbf{h}_{g,\mathbf{y}|\mathbf{x},\boldsymbol{\theta}}].$$

The Jacobian determinant of $\text{vec}(\gamma_{\boldsymbol{\theta}}(\mathbf{z}))$ reduces to $\prod_{g=1}^G |\mathbf{L}_{g,\boldsymbol{\theta}}^{-T}|$.

F Further work

A, by no means complete, list of possible further research directions related to CTHMC processes contains the following:

- More adaptive event specifications in a similar vein to those of Hoffman and Gelman (2014); Betancourt (2016) to obtain trajectory lengths that are better adapted to local geometry of the target distribution. In this regard, working with multiple independent copies of target distribution, with negatively correlated momentums (across the copies) may be useful.
- The results of Section 3 goes through with minimal changes for non-Euclidian Riemann manifold Hamiltonian dynamics (Girolami and Calderhead, 2011) (see Appendix A.4). In this case, the dynamics solve a coupled system of $2d$ first order ODEs (but cannot be reduced to a d -dimensional second order system). In particular, such a development could be carried out with explicit (non-symplectic) numerical integrators for first order systems, which could substantially reduce the often large computational cost of conventional Riemann manifold HMC (see e.g. Kleppe, 2018).
- The recent interest in PDPs is to a large extent motivated by that computationally fast “big data” versions can be constructed without introducing additional approximation errors (see Fearnhead et al., 2018, and references therein). Such “big data” PDPs operates on small randomly selected sub-samples of the data, resulting in so-called stochastic gradients. However, current implementations are restricted to models with few parameters as the deterministic dynamics are generally not adapted to target distribution. The construction of stochastic gradient-versions of the CTHMC processes, which due to adapted dynamics can handle both large models and big data, is one of the main future research questions related to CTHMC processes. More concretely, CTHMC processes do not use the point-wise values of the target distribution itself in e.g. accept/reject steps as in conventional Metropolis-Hastings-based MCMC methods such as HMC. Rather, being a PDP, CTHMC *only probes the target distribution through the gradient of the log-target distribution*. Assuming that the data consist of a large number of independent observations, such gradients can be estimated computationally cheaply and without bias using only subsets of the data (Welling and Teh, 2011; Baker et al., 2019), i.e. using stochastic gradients where the randomness comes from taking random subsamples of the data.
- Recently, pseudo-marginal/transport map MCMC methods (Alenlöv et al., 2016; Kleppe, 2019; Osmundsen et al., 2019) for large scale Bayesian hierarchical models have been proposed. Such methods result in a modified target distribution which “almost” factorizes into a low-dimensional general factor and a high-dimensional standard Gaussian factor. A symplectic integrator optimized for such a situation was developed in Alenlöv et al. (2016). A further development in this project would be to develop a non-symplectic integrator optimized for such “almost factorizing” situations, e.g. using splitting methods (see e.g. Franco and Gómez, 2014).

- It may be beneficial to operate with multiple event rates/momentum refreshes for different parts of the state vector. Theoretically, this should be rather straight forward, but finding good strategies for such a development would require substantial work.
- Reversible variants (based on involutions and reversible jump Metropolis Hastings) using the RKN methodology leads to approximate discrete time MCMC algorithms inheriting many of the properties of CTHMC related to computational robustness. Such algorithms are attractive in that they allow very flexible adaptive selection of the Hamiltonian trajectory (time-)length distribution (e.g. similarly to NUTS). However, their efficient computation requires storing a representation of complete Hamiltonian trajectories and may involve simulation of substantial amounts of dynamics which is only used for calculating accept probabilities (both as opposed to the PDP version).
- A further interesting property of CTHMC processes is that biased (relative to the chosen momentum target distribution $N(\mathbf{0}_d, \mathbf{M})$) updates can be corrected by appropriately chosen event rates. This may be exploited e.g. toward higher momentums intended for jumps between modes, and implemented in a stable manner using the adaptive integrators.